







The interplay between siliciclastic and carbonate depositional systems: Maastrichtian to Danian basin-floor sediments of the mid-Norwegian Møre Basin

Hans Jørgen Kjøll¹  | Ivar Midtkandal¹  | Sverre Planke^{1,2}  | John Millett^{2,3}  | Ben Manton²  | Kresten Anderskov⁴ 

¹Department of Geoscience, University of Oslo, Oslo, Norway

²Volcanic Basin Energy Research (VBER), Oslo, Norway

³Department of Geology and Geophysics, University of Aberdeen, Aberdeen, UK

⁴Department of Geosciences and Natural Resource Management, University of Copenhagen, Copenhagen, Denmark

Correspondence

Hans Jørgen Kjøll, Department of Geoscience, University of Oslo, Oslo, Norway.

Email: h.j.kjoll@geo.uio.no

Funding information

Aker BP

Abstract

Source-to-sink sedimentary systems associated with volcanic rifted margins serve as important archives for basin development by recording lithospheric changes affecting the depositional systems. Distinguishing between sediment transport processes and their sediment source(s) can guide the interpretation of a basin's history, and thereby inform regional paleogeographic reconstructions. In this contribution, we integrate and utilize wireline geophysical logs, detailed petrographic observations from side-wall cores, and seismic analysis to describe and decipher a Maastrichtian to Danian-aged basin-floor depositional system in the deep outer Møre Basin, mid-Norwegian margin. Well 6302/6-1 (Tulipan) is a spatially isolated borehole drilled in 2001 that penetrates Maastrichtian and younger strata. A succession of hitherto undescribed carbonates and sandstones in the outer Møre Basin was discovered. It is investigated for sediment transport, provenance, and depositional processes on the basin floor surrounded by structural highs and ridges. The strata from the lower parts form a basin-floor apron consisting of redeposited carbonate sourced from a westerly sub-aerial high. The apron transitions vertically from mixed siliciclastic and carbonate into a purely siliciclastic fan with intercalated sandstone and mudstone, providing a rare high-resolution record of how depositional environments experience a complete shift in dominant processes. The development coincides with similar latest Cretaceous-earliest Palaeocene sequences recorded south of this region (e.g., well 219/20-1) and may have been influenced by regional uplift associated with the onset of magmatism in the Northeast Atlantic. This study improves our understanding of a late, pre-breakup source-to-sink sedimentary system developed near the breakup axis of an infant ocean, and documents what is possibly the northernmost chalk deposit in the Chalk Group.

KEYWORDS

carbonate basin-floor apron, mid-Norwegian margin, mixed carbonate-siliciclastic deposits

This is an open access article under the terms of the [Creative Commons Attribution](https://creativecommons.org/licenses/by/4.0/) License, which permits use, distribution and reproduction in any medium, provided the original work is properly cited.

© 2023 The Authors. *Basin Research* published by International Association of Sedimentologists and European Association of Geoscientists and Engineers and John Wiley & Sons Ltd.

1 | INTRODUCTION

The evolution of source to sink systems on rifted margins can be complex due to structural elements, such as elongated rotated fault blocks, and isostatic adjustments related to stretching (e.g. Helland-Hansen et al., 2016; Podladchikov et al., 2006; Polanco et al., 2023). For volcanic rifted margins, unravelling sediment routing pathways from shallow waters to deep basins can be even more complex considering the potential role of thermal uplift caused by elevated mantle temperatures, which may expose large areas in the rift axis to sub-aerial erosion (Planke et al., 2022; Walker et al., 2022). Furthermore, late volcanic activity often blankets the outer parts of volcanic rifted margins making seismic imaging in these areas challenging (Millett et al., 2022).

Rift basin architecture affects sediment transport and how sediments accumulate in the sinks as the basin axes are typically parallel to the continent-ocean transition (e.g. Ravnås & Steel, 1998). The source is also important as the distal basins often are cut off from alluvial influx sources, but rather rely on locally sourced sediment with turbidity currents, wind-blown dust, and/or sediments brought in by bottom currents (Ravnås & Steel, 1998). In narrow rift basins, these processes may be overlapping and overprinting, complicating the resultant deposit (e.g. Fonnese et al., 2020). One of the keys to understanding the sediments accumulated in the sinks is therefore the surrounding bedrock and architectural elements of the rifted margin.

In favourable climatic conditions, a significant sediment component can comprise carbonate material, which can be transported into the deep ocean and accumulated either as pure carbonate or as mixed or hybrid sediment with siliciclastic material (e.g. Mount, 1985; Zuffa, 1980). Chiarella et al. (2017) subdivide the mixing of material from active carbonate and siliciclastic systems into (1) compositional mixing and (2) strata mixing. Compositional mixing is found on the scale of a bed when the grains and clasts consist of both carbonate and siliciclastic material. This occurs when the carbonate production is active simultaneously with the influx of siliciclastic material. The latter, i.e. strata mixing, occurs at a larger scale and relates to lithofacies and/or stratigraphic mixing, with an alternation in carbonate/siliciclastic productivity. Lithofacies mixing would occur on an intermediate scale with individual beds of different materials, while stratigraphic mixing occurs on a seismic scale with bed-set packages of alternating carbonate and siliciclastic material.

Carbonate gravity flows are, in contrast to siliciclastic endmembers, generally thought to be triggered from a line of sources fringing the outer platform and accumulate as an apron along the slope of the basin floor (e.g.

Highlights

- Remobilized mixed carbonate-siliciclastic detritus formed a basin-floor apron in the distal Møre Basin.
- A westerly source was likely isolated and shallow marine in the Latest Maastrichtian to Earliest Paleocene during carbonate deposition.
- Carbonate apron was abruptly replaced by a siliciclastic, mud-dominated (Sauetang Member) and sand-rich fan.
- This is the first description of Chalk Group-type sediments in the Møre Basin and extends the chalk group >100 km north.

Mullins & Cook, 1986). Some exceptions occur and, especially in mixed carbonate-siliciclastic systems, calciclastic seafloor fans may develop (Payros & Pujalte, 2008). The fine-grained end-member of the calciclastic seafloor fans can be large (>100 km) and often show poor development of channels as the sediment is often distributed as sheets. Point-sourced carbonate aprons have also been described where the material was channelled from shallow water through gullies and onto the basin floor (Eberli et al., 2019; Reolid et al., 2019; Slotman et al., 2019) in “isolated base-of-slope aprons” (e.g. Tropeano et al., 2022).

The Møre Basin on the mid-Norwegian margin is part of a volcanic rifted margin that underwent several phases of deformation prior to the formation of the volcanic margin and break up in the Palaeocene-Eocene; thus, it had inherited architectural elements from the early rifting as well as the influence from volcanic systems (e.g. Grunnaleite & Gabrielsen, 1995; Skogseid et al., 2000; Theissen-Krah et al., 2017). Three wells penetrate strata in the outer Møre margin (Figure 1), leaving the basin-fill history poorly constrained. Well 6302/6-1 (Tulipan) is located within the center of the basin and penetrates the Cretaceous-Paleogene boundary, which in the mid-Norwegian margin represents the waning stage of a Cretaceous rift episode and the incipient Palaeocene rift stage (e.g. Zastrozhnov et al., 2020). The strata sampled by the Tulipan well presented here documents a significant change in sediment composition and provenance as it shows the evolution from a line-sourced mixed carbonate-siliciclastic system to a point-sourced pure siliciclastic system.

This study documents a hitherto undescribed re-deposited carbonate apron in a spatially isolated well on the mid-Norwegian margin and proposes a depositional model. The model places the spatially isolated

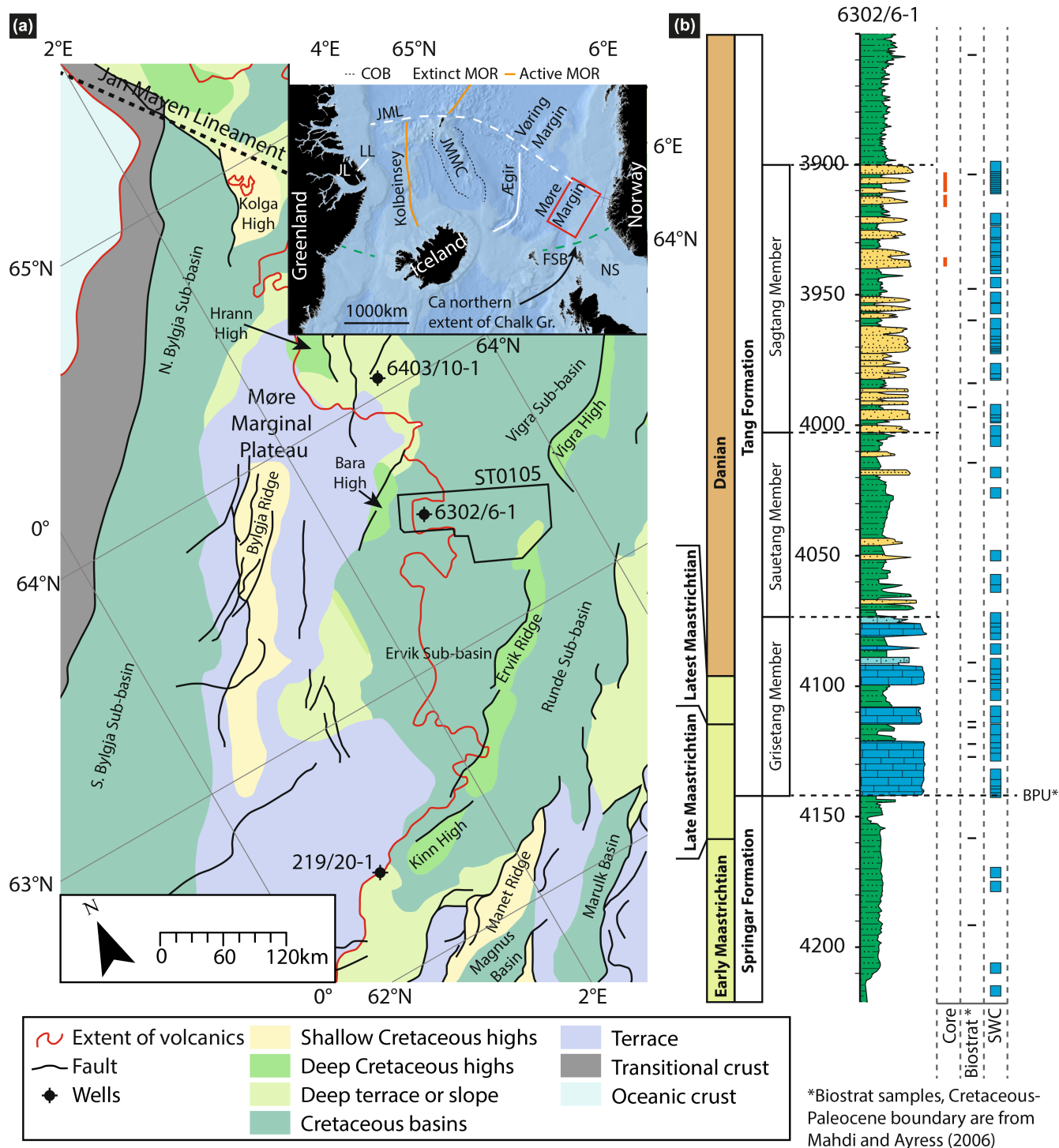


FIGURE 1 (a) Distribution of Cretaceous highs (both shallow and deep) and basins. The map is modified from Gernigon et al. (2021), Millett et al. (2022), and Zastrozhnov et al. (2020). Inset shows the location of the Møre Margin in the North Atlantic realm. The green dashed line on the inset represents the approximate northern extent of chalk deposition in the Late Cretaceous after Surlyk et al. (2003). (b) Lithostratigraphic log based on gamma ray that shows the distribution of lithologies and the new lithostratigraphic subdivision proposed in this contribution as well as sample locations in the well. COB, continent-ocean boundary; FSB, Faroe-Shetland Basin; JL, Jameson Land; JML, Jan Mayen lineament; JMJC, Jan Mayen micro-continent; LL, Liverpool Land; MOR, mid-ocean ridge; NS, North Sea; SWC, side-wall cores.

well data in a regional context and improves understanding of the basin history. We integrate petrographic analyses of side-wall cores with interpretations

of geophysical wireline logs and seismic data from the basin-floor sediments that span the Late Cretaceous to early Palaeocene. A new facies assemblage from

the mid-Norwegian margin is described, consisting of mixed siliciclastic and carbonate sedimentary rocks interlayered with mudstone. In addition to constraining the depositional processes, we subdivide the succession into three new lithostratigraphic members (Grisetang, Sautetang and Sagtang—Norwegian names for varieties of seaweed; [Figure 1](#); [Appendices 1–3](#)) that are assigned to the Tang (Norwegian name for seaweed) formation.

2 | MØRE BASIN GEOLOGICAL SETTING

The mid-Norwegian margin has experienced extension from the collapse of the Scandinavian Caledonides in the Devonian to the final opening of the Norwegian-Greenland Sea in the Eocene (e.g. Mosar et al., 2002). The last phase was accompanied by significant magmatism related to the North Atlantic Igneous Province leading to continental breakup between Greenland and Norway in the Early Eocene (Eldholm, 1991; Eldholm & Grue, 1994; Gernigon et al., 2019). Three main rift episodes are commonly recognized, a Devonian-Carboniferous, a Permian-Triassic, and a final Cretaceous-Paleogene event (e.g. Brekke, 2000; Doré et al., 1999; Peron-Pinvidic & Osmundsen, 2018; Zastrozhnov et al., 2020). The mid-Norwegian margin is commonly subdivided into three segments, the Møre-, Vøring- and Lofoten margins ([Figure 1](#)). The Møre margin is separated from the Vøring margin in the north by the Jan Mayen Lineament (JML). The JML stretches from mainland Norway to E. Greenland ([Figure 1](#)). This fracture zone is also the northern border of the Jan Mayen Microcontinent (JMMC)—a continental sliver consisting of crystalline basement and a cover sequence preserving a Permian/Triassic to Eocene sedimentary succession (Brekke, 2000; Gaina et al., 2009; Peron-Pinvidic et al., 2012; Polteau et al., 2019; Skogseid & Eldholm, 1987). The JMMC rests outboard of the Møre margin, separated by the extinct Ægir Ridge, which initiated in the Eocene at magnetic anomaly C24r ([Figure 1](#); Gernigon et al., 2012). To the south, the Møre margin borders the Northern North Sea and the Faroe-Shetland Basin (FSB; [Figure 1](#)).

Through the Cretaceous, the Møre Basin generally consisted of deep sub-basins separated by narrow, elongate structural highs that locally are thought to have been exposed above sea level (e.g. the Kolga High; Gernigon et al., 2021; Planke et al., 2022; [Figure 1](#)). The sub-basins locally host thick Cretaceous strata of >8 km thickness, primarily mudstone with minor turbiditic

sandstones and carbonate stringers (Blystad et al., 1995; Brekke, 2000; Dalland et al., 1988; Vergara et al., 2001). Two prominent ridges, the Bylgja Ridge and the Ervik Ridge, separates the Bylgja Sub-basin to the west from the Ervik Sub-basin in the center and the Runde Sub-basin to the east ([Figure 1](#)). Paleo-bathymetric studies suggest that the water depth around the late Cretaceous to Early Paleogene ranged around 150–300 m, but is complicated by the uncertainty regarding the effect of dynamic support from an anomalously hot mantle (Kjennerud & Vergara, 2005; Roberts et al., 2009; Sømme et al., 2023; Wien & Kjennerud, 2005). The mid-Norwegian margin underwent basin inversion throughout the Cenozoic which formed domes, such as the Helland-Hansen Arch (e.g. Doré et al., 2008).

The Cretaceous succession is abruptly terminated in a margin-wide unconformity, the Base Paleogene Unconformity (BPU), which, in the FSB has been attributed to either inversion structures in the late Cretaceous/early Palaeocene (Booth et al., 1993) or caused by transpressional reactivation of major NE trending faults (Goodchild et al., 1999). Stoker (2016) further suggests that the BPU is an erosional boundary, but that a local conformable transition cannot be ruled out in the FSB area (Lamers & Carmichael, 1999). In the Møre Basin, the BPU is overlain by the Paleocene-Eocene-aged Tang Formation, which is described as primarily consisting of mudstones with locally some turbiditic sandstone units (Dalland et al., 1988). Paleogene limestone, on the other hand, have not been previously reported in the Møre Basin, as the Maastrichtian Chalk Group is commonly accepted to terminate in the northern North Sea ([Figure 1](#); e.g. Surlyk et al., 2003).

Three wells are drilled in the distal Møre basin: 6302/6-1 (Tulipan), 6304/10-1 (Solsikke) in the Norwegian sector and 219/20-1 in the UK sector ([Figure 1](#)). The Tulipan well is one of the few wells in the Norwegian Sea drilled in a basin depocenter rather than on an underlying structural high, which has yielded an expanded Palaeocene stratigraphy.

3 | DATA AND METHODS

3.1 | Well data

The Tulipan well, a vertical exploration well drilled in 2005, penetrates down to Maastrichtian mudstones at 4234 m MD RKB (measured depth below the rotary kelly bushing, 29 m above mean sea level), terminating c. 400 m above a saucer-shaped sill (Kjøberg et al., 2017; Schmiedel et al., 2017). All depths referred

TABLE 1 Average P-wave velocities used in the time-depth conversion.

Formation and member	Well tops TVDss (m)	Average interval V_p (m/s)
Seawater		1482
Seafloor (top Naust Formation)	1286	1957
Kai Formation	2463	1957
Brygge Formation	2582	1957
Tare Formation	3223	2317
Tang Formation	3395	2346
Sagtang, Sautang and Grisetang Member	3901	2738
Springar Formation	4080	3004

Note: Depths are given in true vertical depth subsea (TVDss).

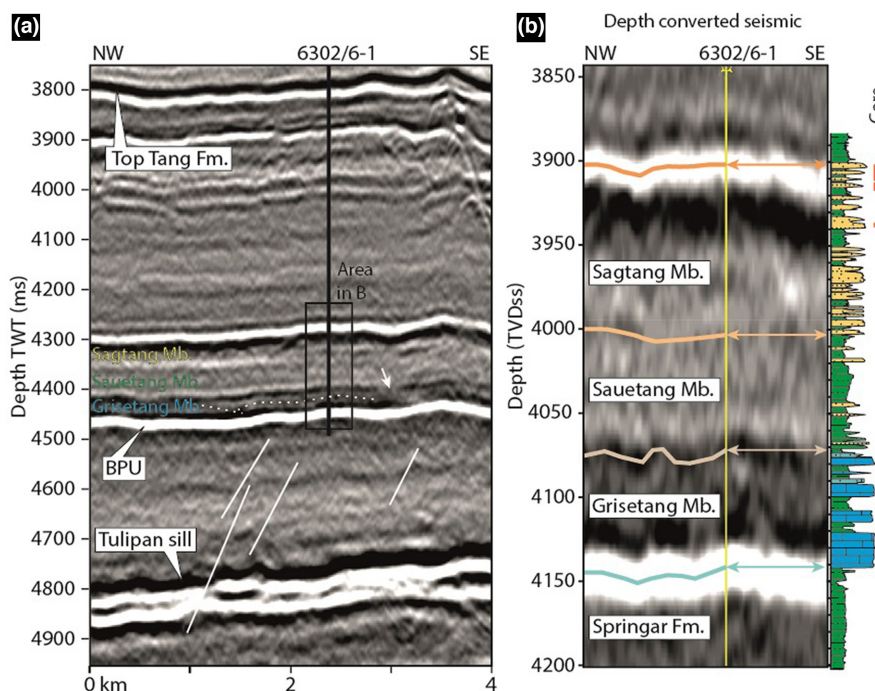


FIGURE 2 (a) Detail of a 2D seismic line crossing the Tulipan well 6302/6-1 (see Figure 1 for location), where the seismic facies are defined. White arrow highlights transparent areas in the top of the Grisetang Member, whereas thin, white dashed lines within the Grisetang Member show discordant internal reflections. The white lines below the BPU show small-scale faulting in the Cretaceous mudstones, locally offsetting the Tulipan sill. (b) Depth converted seismic section of the key area. The Sautang Member is poorly defined in the seismic section since it is defined primarily due to the higher abundance of mudstones than the overlying Sagtang Member. The top of the Sagtang Member is defined to be the reservoir sandstone, which is an intra-Tang Formation reflector. Top of Grisetang is defined as a hard reflector at the occurrence of the first mixed carbonate siliciclastic bed. BPU, Base Paleogene Unconformity.

to within this contribution are MD RKB unless otherwise stated.

The available sampling program from the drilling operations included a full conventional wireline logging suite including calliper, natural gamma ray, resistivity, neutron porosity, density, and sonic tools, along with Formation Micro Imager (FMI) data. The wireline data coverage and quality is generally very good; however, minor exceptions occur leading to data gaps, especially for the FMI log. Image log data are susceptible to borehole wall artefacts, such as drilling-induced fractures

and drill bit marks, which can complicate interpretation. Care was taken to avoid obvious artefacts; however, the potential for interference from such features when interpreting geological features cannot be fully mitigated. Where the FMI data are missing, other geophysical data are present. Depth-matching and correlation between logging tools is generally good with only minor depth-shifts required over the investigated interval. The lithologies in the lithological column was interpreted based on a simple gamma ray cut-off for 'sand-prone' versus 'mud-prone' lithologies. The cut-off value was set at 25% of the

maximum GR value and compared and adjusted according to the lithologies from the sidewall cores (SWC).

Cuttings were sampled by the operator at 10 m intervals from 3150 to 3850 m and at 3 m intervals from 3850 m to terminal depth. A total of 15.7 m of discontinuous core was recovered between 3903 and 3942 m (Figure 1). All three core segments are from the reservoir unit, a Danian-aged sandstone interval from the Sagtang Member. The core has not been studied in detail for this contribution. 121 SWC were collected mainly from the reservoir level (3901 m) and down to Top Springar Formation (4080 m; Figure 1), from which thin sections were made available.

Micropaleontologic and palynologic analysis has been carried out for the entire well (Mahdi & Ayress, 2006) and is available from the Diskos database (The Norwegian National Data Repository for Petroleum Data). The Cretaceous-Paleogene boundary is proposed to be between 4098 and 4089 m, as constrained by the first occurrence of a persistent Palaeocene agglutinated foraminifera and the last occurrence of two latest Maastrichtian foraminifera (Mahdi & Ayress, 2006; Figure 1).

The well data and samples presented in this contribution are from a 331 m thick interval, between 4231 and 3900 m. Petrographical and petrological investigations were performed on thin sections and from cuttings sampled specifically for this study. Both optical microscopy and scanning electron microscope—energy dispersive spectrometer (SEM-EDS) analyses were used to characterize the thin sections and for mineral identification.

3.2 | Seismic data

The seismic data used for this study is the 3D cube ST0105—a full-stack, time-migrated, zero-phase data set processed in 2001. It covers an area of 1610 km² within the western Møre margin (Figure 1) with a line spacing of 12.5 m. It was recorded to a depth of 7 s two-way travel-time (TWTT). In the presented seismic lines, an increase in acoustic impedance (i.e. hard reflections) are black, whereas a decrease in acoustic impedance (i.e. soft reflections) are white. Down well-bore geophones was used to generate a vertical seismic profile (VSP) time-depth curve (Table 1; Figure 2), which in turn was used to develop a layered velocity model based on the interval velocities. This was later used to convert key seismic horizons from time to depth and produce thickness maps (Table 1; Figure 2). The area of interest for this study is relatively deep at c. 3600 to 4100 m depth.

The vertical seismic resolution was calculated using the dominant frequency volume attribute in the Petrel software (SLB). Furthermore, by using the mean

amplitude attribute between Top Sagtang and the BPU, a mean amplitude value of 29,58 Hz was extracted from the surface statistics. The vertical resolution was thereby deduced using the relationship $\lambda = v/f$, where λ is the seismic wavelength in meters, v is the interval velocity in m/s and f is the frequency in Hz (1/s). The interval velocity at the depth of interest is 2738 m/s and the mean amplitude is 30 Hz, which gives a wavelength of 93 m. By using the definitions of vertical seismic resolution given in Simm and Bacon (2014) of tuning limit at $\lambda/4$ and detection limit at $\lambda/30$ we have vertical resolutions at 23 and 3 m, respectively. The horizontal resolution is generally taken as the larger value of $\lambda/4$ or the line spacing; thus, for this study, the horizontal resolution would be 23 m (e.g. Lebedeva-Ivanova et al., 2018).

4 | RESULTS

4.1 | Thin sections and wireline logs

4.1.1 | Springar Formation

The upper Springar Formation (Figure 1) was sampled by the Tulipan well and the wireline logs show geophysical characteristics, such as an average V_p of 2.81 ± 0.1 km/s, average GR of 99.7 ± 9.2 API and density averaging at 2.49 ± 0.03 g/cm³ (Figure 3a; Table 2), consistent with their mudstone nature. The FMI data, together with the other wireline logs suggest laminated, fine-grained and clay-rich sediments (Figure 3a,b) that are locally affected by bioturbation. Locally the FMI reveals a discordant fabric in the mudstones (Figure 3b). Although the Springar Formation is relatively homogeneous, the uppermost 7 m shows a slight increase in V_p towards the BPU (Figure 3a).

In total, seven thin sections from SWC were investigated revealing mudstones with some silt-sized clastic domains primarily comprised of angular to sub-angular, fine-grained (100–200 μ m) quartz grains with minor feldspar, muscovite and biotite suspended in a muddy matrix (Figure 3c–e). Locally, abundant euhedral pyrite is present. Glauconite pellets are also common and in one thin section, they show a wide range of grain sizes and shapes (Figure 3e). In sample 4150.2, the clasts are embedded in a chert matrix (Figure 3c,d).

4.1.2 | Interpretation of the data from the Springar Formation

The sampled part of the Springar Formation is interpreted as the distal part of a siliciclastic turbidite system

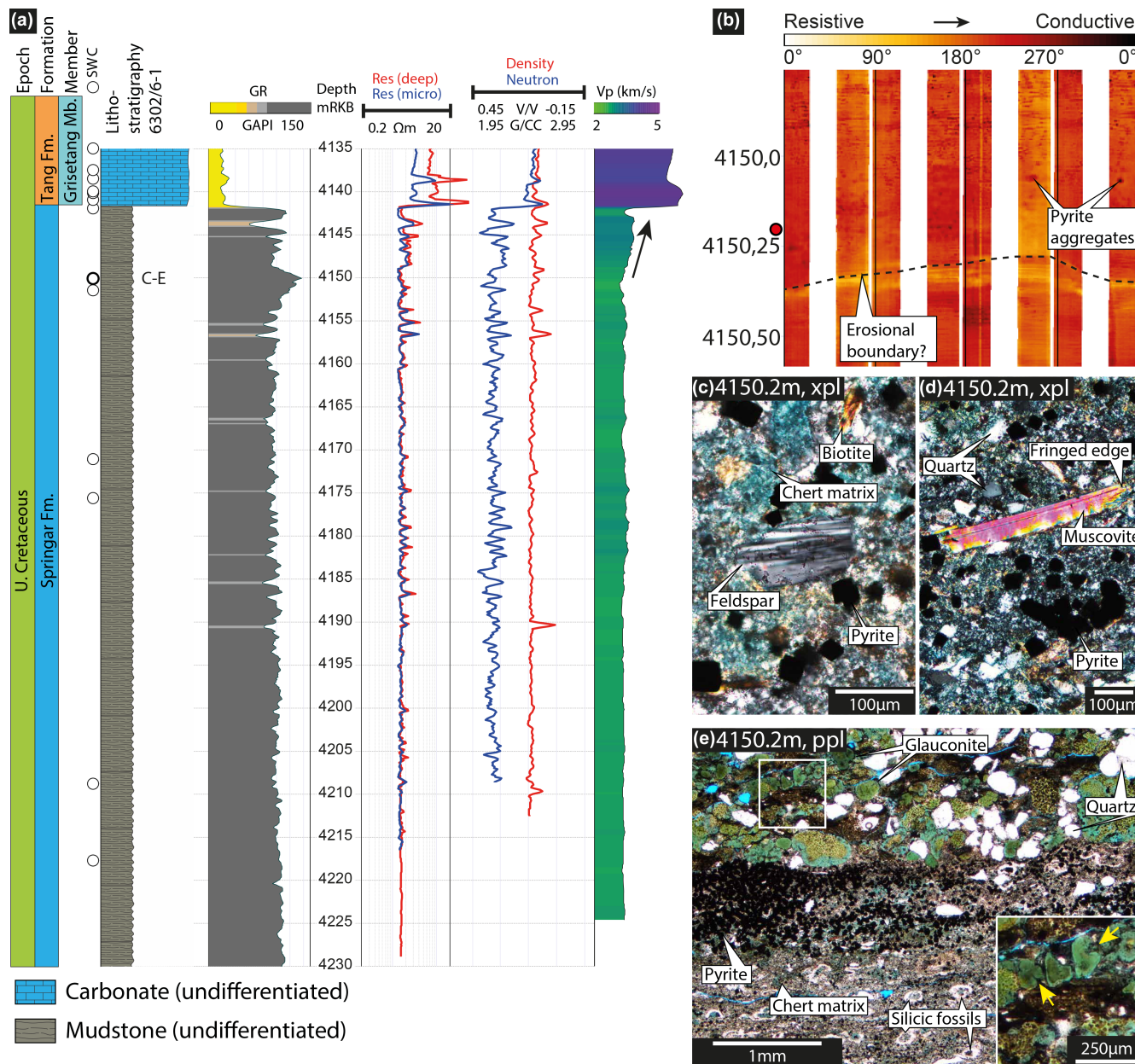


FIGURE 3 Overview of the Springar Formation (a) V_p and GR show typical mudstone characteristics (high GR and low V_p compared to carbonate). Note the slight increase in V_p for the upper 7 m of the Springar Formation. The location of SWC samples and FMI data are shown next to the lithostratigraphic column. (b) FMI data from the well shows typical resistivity textures from the Springar Formation. The boundary between the two is irregular and perhaps reflects erosion during deposition of the upper facies or post-deposition soft sediment deformation. Note the red circle, which indicates the location of SWC 4150.2, presented in b. (c) Photomicrograph from a SWC sample shows a feldspar and biotite grain embedded in a matrix of chert and with secondary euhedral pyrite crystals. (d) Photomicrograph that shows a muscovite grain with fringed edges, typical for detrital muscovite. It is set in a cherty matrix with silt-sized quartz grains. (e) Photomicrograph displaying a relatively large muscovite grain with fringed edges typical of detrital mica. (f) Photomicrograph showing a layered sequence rich in complex glauconite pellets. Yellow arrows indicate craquelures. The lower part is a silicified domain rich in silicic microfossils and pyrite in a chert matrix. xpl: crossed polarized light, ppl: plane polarized light.

in accordance with, e.g., Dalland et al. (1988), where most of the detritus is siliciclastic mud with minor input of siliciclastic grains (Figure 3c–e). The discordant fabric observed in the FMI data may represent the erosion between

two turbidite flows or post-depositional soft-sediment deformation (Figure 3b). The glauconite grain size- and shape variation (Figure 3e) indicate periods of non-deposition in the area (Amorosi, 1997).

TABLE 2 Average values for the Upper Cretaceous to Lower Eocene in the Tulipan well.

Depth	Formation	Member	Lithology	n	Average								
					Thickness [m]	GR	σ	Density	σ	Neutron	σ	V_p	σ
3901	Tang Formation	Sagtang Member		19	1.1	50	4	2.33	0.06	0.25	0.02	2.9	0.1
					4.6	87	11	2.40	0.05	0.31	0.03	2.8	0.1
3997.6		Sautetang Member		7	11.4	91	12	2.42	0.04	0.34	0.04	2.8	0.1
					0.8	45	6	2.47	0.04	0.22	0.04	3.0	0.1
4074		Grisetang Member		5	6.7	31	6	2.53	0.03	0.17	0.04	3.8	0.1
					1.9	32	11	2.54	0.05	0.20	0.10	2.9	0.0
					5.8	55	22	2.55	0.03	0.12	0.02	4.0	0.4
					5.8	27	7	2.52	0.03	0.14	0.04	3.7	0.1
					20.6	22	2	2.53	0.04	0.14	0.03	4.2	0.1
					3.2	39	8	2.46	0.02	0.23	0.04	3.6	0.1
					1.3	42	9	2.45	0.03	0.24	0.07	3.5	0.2
					3.4	25	6	2.53	0.02	0.15	0.04	3.7	0.1
					1.2	30	14	2.50	0.02	0.17	0.03	3.9	0.0
					13	84	9	2.46	0.03	0.28	0.04	3.0	0.1
4141.7	Springar Formation			1	89+	100	9	2.49	0.03	0.33	0.03	2.8	0.1
TD: 4231													

Note: σ : Std. deviation. C1–C4 Carbonate unit 1–4, Mixed 1–3: Mixed carbonate-siliciclastic beds 1–3. Yellow: Sandstone, Green: Mudstone, Blue: Carbonate, Gold: Mixed carbonate-siliciclastic.

4.1.3 | Grisetang Member (Lowermost Tang Formation)

The Grisetang Member is mixed, consisting of carbonate, mudstone and minor fine-grained arkosic sandstone. It has a total thickness of 68 m in the Tulipan well. Internally, it contains four intervals of distinct geophysical properties, each between 0.6 and 19 m thick (Figure 4). These intervals are composed of carbonate, mainly very fine-grained micritic limestone (wackestone) and sandstones interlayered by mudstone. The sandstones become more frequent up section together with the demise of the micritic limestone. For convenience, the two uppermost carbonate layers are described as C4 and the carbonate layers are referred to as C1–C4. C3 and C4 are directly overlain by sandstone (Figure 4). The rocks present in the Grisetang Member can be subdivided in 4 lithofacies (Table 3).

4.1.3.1 | C1 carbonate layer 1

The lowermost carbonate unit (C1) is 20.75 m thick (4141.75–4121.00 m) and represented by ten SWC (Table 2 and Figure 4a). It is deposited directly onto the BPU. The average V_p and GR is 4.17 ± 0.08 km/s and 21.51 ± 2.49 , respectively (Table 2). There is some variability within the unit especially in the lower 4 m (4142–4138 m) where there are two distinct positive peaks in resistivity and density with corresponding negative peaks in neutron porosity (Figures 4a and 5a).

The central part of C1 is poorly mapped by the FMI due to tool sticking, but the lowermost and uppermost parts are mapped and allows FMI interpretation. The lowermost part shows alternating, thick (dm-scale) bands of low and high resistivity. Locally, at c. 4138.5 m a feature resembling cross stratification or soft sediment deformation can be observed. The feature is truncated at the top by a conductive layer (Figure 6a). At 4138 m, a transition to a more homogenous FMI signal occurs. Here, the carbonate appears to be divided into decimetre- to meter-thick beds separated by thin layers with low resistivity. Internally, the beds are rather uniformly resistive, but commonly with thin lamination. The thickness of the beds in the C1 layer increase upward and range from 0.1 to 1.8 m (Figure 6e).

Based on observations of SWC and wireline log patterns the lower two meters are a normal graded section of packstone overlain by an 18 m thick homogenous micritic limestone, of which the uppermost 5 m are normally graded (Table 3; Figure 5). SEM reveals that the micritic component consists of partially recrystallized very fine-grained fossil fragments, such that the state of fossil preservation is poor but a few identifiable coccoliths and echinoids occur (Figure 4f).

C1 show a clear homogenization trend where the variety of fossils transition from a rich fauna including bryozoans, foraminiferas and bivalve fragments to a less diverse fauna only including calcispheres and some bivalve fragments (Figure 5b–e). In the lower part, in addition to the diverse microfossil fauna, it also consists of relatively coarse (<2 mm) and well-rounded sand grains mainly consisting of quartz (Figure 5b,c). Towards the top the fossil fauna is virtually only composed of foraminifers with some sparse bivalve fragments defining a fabric in the rock (Figure 5d). The calcispheres sizes decrease towards the top of the sub-unit. Siliciclastic grains become less abundant towards the top (from c. 20% in the lower part to <1% in the upper part) and in the uppermost sample they are scarce. The same pattern can be observed for glauconite pellets which are common in the lower part of the sub-unit but disappears towards the top (Figure 8).

The upper sub-unit consists of a homogenous package of very fine-grained micritic limestone (Table 3). The microfossils are primarily calcispheres or fragments thereof, fragments of echinoids, including spines, and agglutinated foraminiferas suspended in the micrite (Figures 4f and 7a). Half-circle fragments of calcispheres show a preferred orientation and form a fabric in some of the thin sections, but no consistent convex/concave up/down distribution is recorded (Figure 4f). Only a handful of microfossils are crushed in situ, i.e. most of the microfossils were either crushed before they reached their final resting place or are intact. Most of the calcispheres and other foraminifers are completely or partially filled with framboidal pyrite, with no observed consistent up/down pattern (Figure 5). Silt to fine sand-sized siliciclastic fragments, primarily composed of quartz, feldspar (both K-feldspar and plagioclase) and mica (primarily white mica), are most common in the lower part and decrease in abundance towards the top of this upper sub-unit, but small (<30 μ m) siliciclastic grains and <50 μ m bioclastic grains are observed throughout (Figure 5e). SEM studies show that there is a very low concentration of clay minerals in the micritic limestone, as also indicated by the GR signal (Figures 4a and 7a).

Locally, the SWC sample thin (from c. 2 mm to >1 cm) internally persistent argillaceous horizons. These contain silt-sized angular siliciclastic grains, primarily composed of quartz and feldspar, as well as small (<100 μ m long axis) flakes of white mica (presumably muscovite), calcispheres and elongated fossil fragments, possibly bivalves (Figures 4d and 5c). These grains are both more abundant, but also larger than those in the micritic limestone.

4.1.3.2 | C2 carbonate layer

Carbonate layer C2 occurs between 4114.1 and 4108.3 m and is 5.8 m thick (Figure 4). It consists of fossiliferous

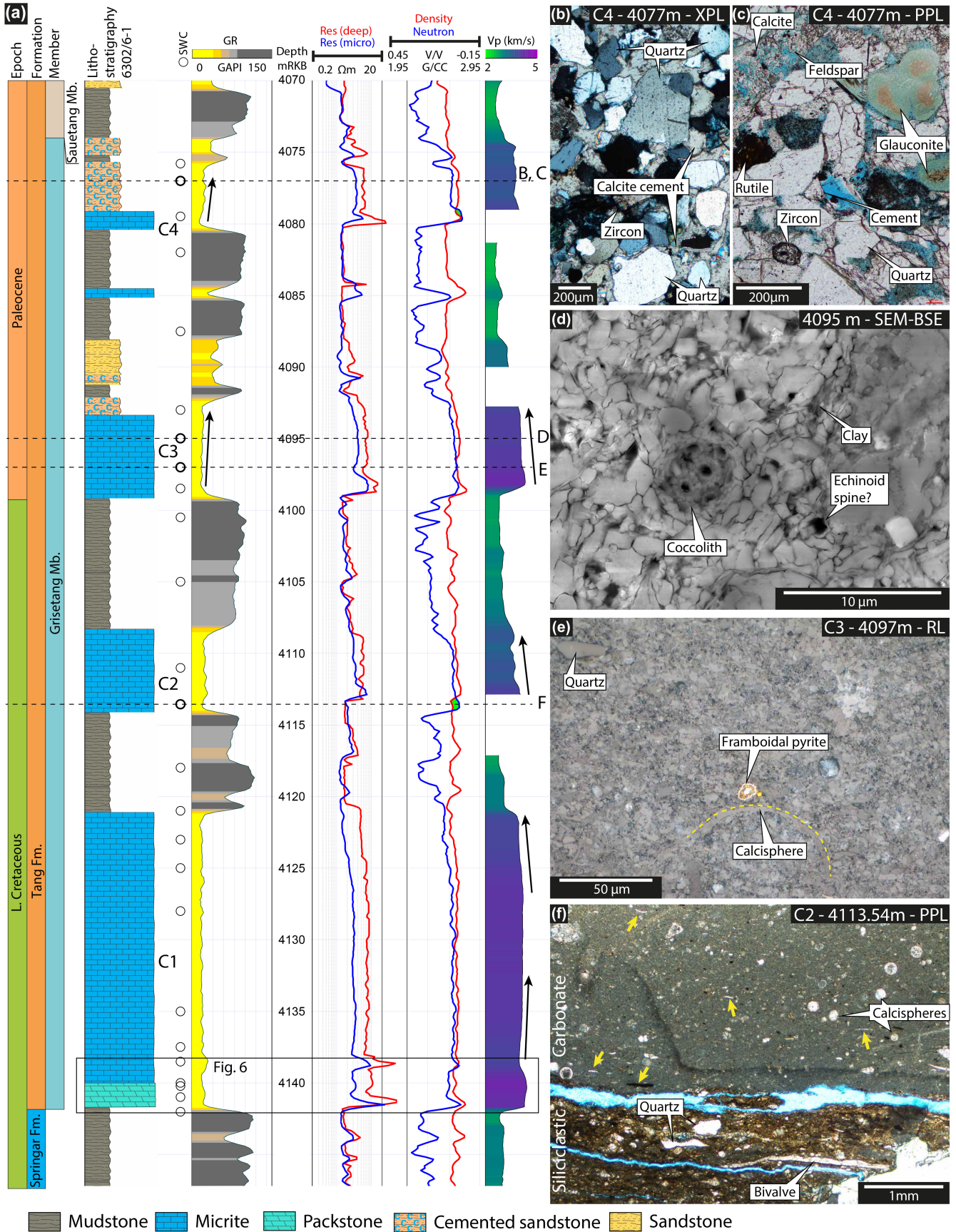


FIGURE 4 Wireline geophysical properties and photomicrographs of lithologies for Grisetang Member. (a) Carbonate layers are denoted C1–C4. Arrows indicate trends in data. Dashed lines indicate sample location of thin section with photomicrograph b–e. (b) Photomicrograph of calcite cemented sandstone with low GR and relatively high V_p . Note the bimodal clast shape distribution with both angular and rounded grains. Sparry calcite cement with single crystals encapsulating several detrital grains. (c) Photomicrograph of the same sample as in b. Zircon and rutile are accessory minerals. Glauconite pellets are common. Feldspars are partially dissolved and filled with calcite. (d) Backscattered electron image of the micritic limestone with a coccolith fossil and crosssectional cut of echinoid spine. (e) Photomicrograph taken with reflected light displaying very fine-grained micritic limestone with crescent-shaped calcispheres fragments. Detrital quartz grains are present together with framboidal pyrite and other sulphides. (f) Thin bed of siliciclastic material in the micritic limestone. The siliciclastic layer is c. 5 mm thick. Yellow arrows indicate grains with a high aspect ratio that define the bedding in the sample. Note that fossil fragments and detrital grains generally are larger in the siliciclastic bed. GR, gamma ray; PPL, plane polarized light; Res, resistivity; RL, reflected light; SWC, side-wall core; XPL, crossed polarized light.

micritic limestone. The wireline logs show a basal interval characterized by low GR, resistivity, porosity, and density overlain by an approximately 5 m thick interval with an upward increasing porosity accompanied by decreasing acoustic velocity (V_p) and density (Figure 4). These observations suggest a basal, coarse-grained (poor in clay minerals) bed succeeded by a fining-upward succession or normal graded bed.

The top and base of the carbonate layer suffered tool-sticking and the contacts are therefore not covered by FMI. Similarly to C1, this carbonate layer is based by dm-scale alterations between conductive and resistive layers before transitioning abruptly upwards into homogeneous beds separated by conductive boundaries. Locally the boundaries show a sinusoid geometry, indicating that they are inclined (Figure 6b). The thickness of the beds increase upward in the carbonate layer and range from 0.2–0.9 m (Figure 6e).

Two SWC were collected and revealed a composition of very fine-grained micritic limestone with argillaceous horizons (Figure 4d). The fossils are primarily calcispheres, agglutinated foraminifera and fragments of echinoids along with fragments of the above-mentioned microfossils (Figure 4). Minor occurrences of siliciclastic grains mostly comprising very fine-grained (<30 μm) quartz, rutile and muscovite are recorded (Figure 4). Some larger (<0.5 mm) fossil fragments are also observed, oriented parallel to the boundary of the argillaceous horizon.

4.1.3.3 | C3 carbonate layer and accompanying sandstone

Carbonate layer C3 is 5.8 m thick (4099.2–4093.3 m) and consists primarily of fossiliferous micritic limestone, which is sampled by 3 SWC. It is overlain by 1.2 m of a siliciclastic sandstone with no mud (4092.1–4093.3 m) sampled by 1 SWC (Figure 4). The average V_p and GR signal is 3.95 ± 0.35 km/s and 54.80 ± 21.50 API, respectively. GR displays a minor increase upwards, which probably reflects the increasing siliciclastic or glauconite

content. Neutron porosity increases upwards and is accompanied by decreasing resistivity, density and V_p .

The data from the lower half of C3 are obscured by tool sticking and hinder analysis. It does, however, appear to be relatively conductive and resembles the same pattern observed in the lower part of C1 and C2. The upper part of C3 consists of similar beds as described above with thin resistive boundaries. Some of the beds also have internal laminations. Locally these laminations are inclined giving a resemblance to small-scale dunes or cross-stratification (Figure 6c insert 3). The bed boundaries are locally inclined and in one instance truncated by the boundary above (Figures 6c insert 1 and 2). In the uppermost part of C3, a 1 m thick calcite cemented sand layer reveals a very similar FMI signature and is indistinguishable from the underlying carbonates in terms of resistivity. The beds thicken towards the top of C3 with thicknesses ranging from 0.1 to 1 m (Figure 6e).

The lower part of C3 consists of micritic limestone with some siliciclastic grains primarily comprising quartz, feldspar and mica. Calcispheres are also common. Siliciclastic grains are more abundant higher in the section. The uppermost part of C3 consists of a relatively coarse-grained sandstone with siliciclastic fragments consisting of quartz, feldspar (both plagioclase and K-feldspar) as well as lithic fragments. The grain-size distribution is roughly bimodal with coarse-grained (>500 μm), rounded clasts and finer-grained (<200 μm) angular clasts. Accessory detrital clasts/minerals are carbonate, chert, biotite, muscovite, rutile and relatively coarse (100–200 μm long axis) idiomorphic zircon. Glauconite pellets (<500 μm) are also present. The sample shows low compaction and is clast-supported. The porosity is, however, entirely occluded by a micritic matrix, which is partially recrystallized as sparry carbonate cement (Figure 7d). Some of the feldspar grains are partly dissolved. The voids created by this dissolution are filled by sparry carbonate (Figure 7d). No argillaceous mud has been observed in this sample, except for mm-sized clasts of clay-rich material, resembling rip-up clasts (Figure 7b).

TABLE 3 Lithological facies in the Grisetang Member.

Grain types		Wireline log characteristics						
Facies	Skeletal component	Detrital component	Matrix/Cement	Sedimentological features	GR	Resistivity	V_p and density	Interpretation
Graded packstone	Bryozoan, bivalve fragments, calcispheres, foraminifera	> 10% fine sand to silt. Quartz, feldspar Phyllosilicates. Glauconite	Micrite	Massive at base and transitions to laminated. Normally graded	Low GR with average 23 API	Very High to high	Very high to high	Calciturbidites or basal part of carbonate dominated gravity flows
Laminated micritic limestone (wackestone)	Calcispheres, coccolith, foraminifera, echinoids undifferentiated nanofossils	Quartz silt, fine grained (<100µm phyllosilicates). Glauconite. Some clay	Micrite	Some lamination. Bedded. Locally erosive bed boundaries.	Low GR with average 26 API	High	High	Carbonate dominated gravity flows
Sandstone (Arkose)	Calcispheres, foraminifera, bivalve	Quartz, feldspar, phyllosilicates, glauconite, rutile, zircon. Bimodal grain size and rounding	Locally sparry cement, quartz-illite matrix or siderite rhombs. <5% quartz cement	Crossbedding. Erosive bed boundaries. Bimodal grain size and grain rounding	Relatively low GR with average 38 API	Medium	Medium	Clean sand with very little mud
Bioturbaded Mudstone	Calcispheres, bivalve fragments	Angular quartz silt and phyllosilicates. Glauconite	Siliciclastic mud	Burrows	High GR with average 83 API	Low	Low	Hemipelagic suspension settling

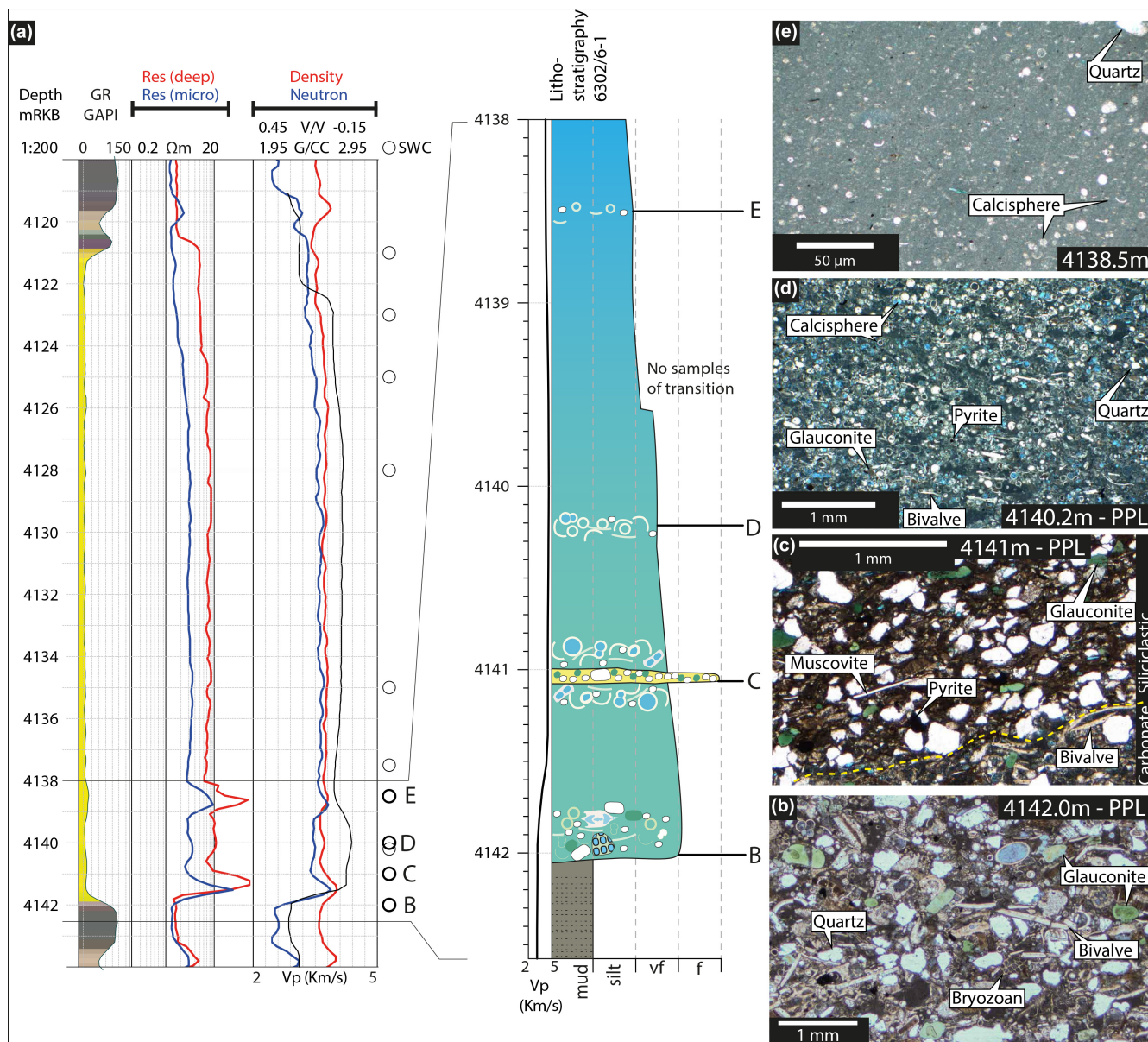


FIGURE 5 Base of the Grisetang Member shows a transition from massive packstone to laminated packstone to very fine-grained micritic limestone. (a) Wireline log shows the geophysical character of the lowermost part of the Grisetang Member. Note the complex pattern of the graphs for the lowermost part which is depicted in the log to the right. (b) to (e) Photomicrographs displaying the mineral assemblages from the lowermost part of the unit where it develops from a mixed carbonate and siliciclastic to micritic limestone. (b) Packstone with c. 20% siliciclastic grains and a plethora of microfossils including fragments of bryozoans and bivalves. (c) Locally argillaceous horizons are present. These are rich in siliciclastic grains primarily quartz, but also detrital muscovite. (d) Packstone primarily consisting of calcispheres and bivalve fragments defining a fabric. (e) Micritic limestone (wackestone) with abundant calcispheres, both intact and half-circle fragments. Some siliciclastic grains are present.

4.1.3.4 | C4 carbonate layer and accompanying sandstone

The two micritic limestone layers that constitute C4 has an accumulated thickness of c. 2 m of micritic limestone (between 4085.1 and 4084.5 m and 4080.2 and 4079.1 m for the lower and upper layers, respectively) and is sampled by 1 SWC. It is overlain by c. 4.6 m of siliciclastic sandstone with little mud (4079.1–4074 m), sampled by 2 SWC (Figure 4).

The wireline logs from the lowermost carbonate layer in C4 show a distinctive reduction in GR and increase in V_p . The FMI reveals that the lowermost carbonate layer in C4 has two beds, with a relatively resistive nature compared to the beds in, e.g., C3. The two beds are separated by a thin (c. 10 cm) layer of more conductive lithology. The FMI for the C4 shows a weak dm-scale resistive banding and sinusoidal conductive bed boundaries, which increase in amplitude towards the

top (Figure 6d). The base of the layer shows a discordant relation to the underlying mudstones (Figure 6d). The beds thicken upward and range from 0.25 to 1 m (Figure 6e).

The GR and V_p signal for the upper C4 carbonate layer increase and decrease, respectively, towards the top of the layer (Figure 4). The lowermost 1.4 m show an increase in resistivity as well as a decrease in neutron porosity to below the density curve (Figure 4). The FMI shows an irregular and discordant boundary between the underlying mudstones and the carbonate, suggesting that the substratum may have been eroded. The lowermost meter shows a clear dm-scale resistive banding before transitioning sharply into the homogenous pattern with well-defined beds (Figure 6d). This transition apparently also corresponds to the lithological change from micrite to carbonate cemented sandstone. The boundaries in the sandstone are generally not defined by one thin line, but rather by numerous densely spaced conductive boundaries (Figure 6d). The homogenous, internal domains show a faint discordant fabric (Figure 6d).

Both of the carbonate layers of C4 are composed of fossiliferous micritic limestone, relatively rich in microfossils such as calcispheres and agglutinated foraminifera. Elongated fossil fragments define a planar fabric in the sample.

Seemingly conformably above the micritic limestone rests the sandstone with similar features as described for the sandstone above C3. The main clast types are quartz (sometimes with textures indicating dynamic recrystallization; Figure 7b,d) and feldspar (both K-feldspar and plagioclase). Accessory clasts and minerals are biotite, muscovite, chert, rutile and idiomorphic and rounded zircon (Figure 4b,c). Glauconite is present in all thin sections (Figure 4c). Feldspar grains are partly dissolved and filled with single crystals of carbonate (Figure 7d). These sandstone samples also have a clear bimodal grain-size distribution where the large grains appear more rounded than the fine-grained fraction (Figure 7b). The samples

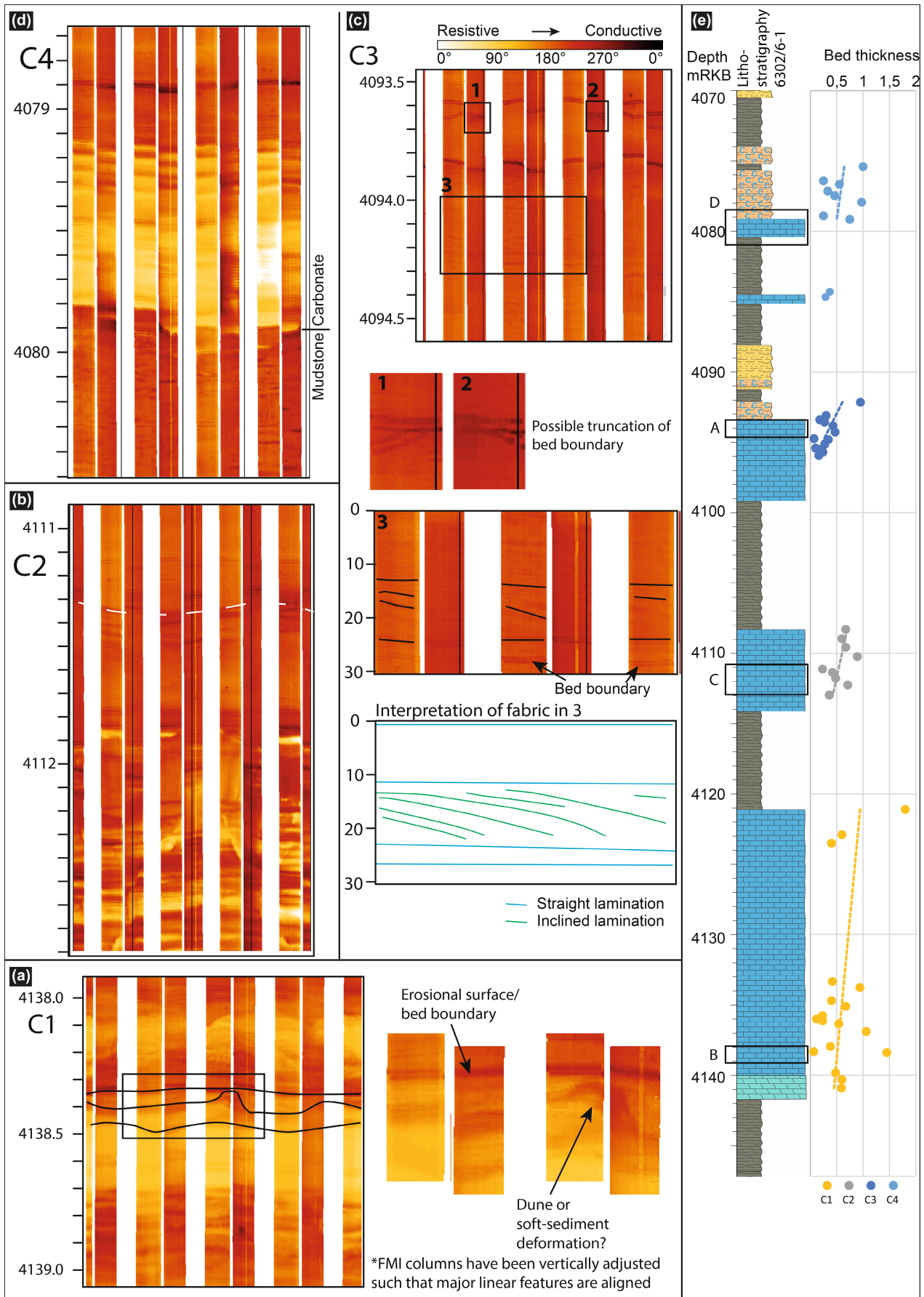
are partially cemented, and the cement is composed of sparry carbonate forming large, single carbonate crystals, which encapsulate several 10's of siliciclastic and carbonate grains (Figure 7d), or fine-grained (<5 μm) quartz and clay minerals (perhaps illite; Figure 7c).

4.1.4 | Interpretation of the data from the Grisetang Member

The carbonates of Grisetang Member are primarily chalks, with subordinate packstone dominated by similar microfossils assemblage as in the chalk. The benthic microfossils, such as bivalves and echinoids found in C1–C4 suggest a shallow marine origin (e.g. Surlyk, 1997). The trends observed in the wireline logs probably represent a thickening- and fining-upward stacking pattern of micritic limestone beds separated by thin layers of argillaceous material interpreted as hemipelagic mudstone beds (Figure 6e). Alternatively, each carbonate bed could be interpreted as representing a single depositional event resulting in thick normal graded units. The FMI data reveal a faint lamination fabric internally in some of the beds which probably formed by deposition from turbidity currents (Anderskov & Surlyk, 2011; Damholt & Surlyk, 2004). This fabric is locally discordant to the bed boundaries and is interpreted to potentially represent bed forms (Figure 6c). The preservation of lamination suggests that the material was not affected significantly by bioturbation and thus either suggests dysoxic conditions at the sea floor during deposition (Damholt & Surlyk, 2004) or rapid deposition, which impeded bioturbation (Scholle et al., 1998).

Calcispheres are either intact or half-moon shaped, but they are rarely observed to be crushed in situ, suggesting that there has been a component of post-mortem transport. Glauconite pellets are abundant in the coarser limestones at the base of C1, in the argillaceous horizons that define the beds and in the siliciclastic sandstones in the

FIGURE 6 Key FMI observations from the Grisetang Member. The FMI scale is the same for all the subfigures and is given in C. (a) FMI data from C1 show what resembles climbing ripples truncated by an erosional bed boundary. (b) FMI data from C2, displays different facies of FMI signal that can be observed. Note the more conductive bands in the lower part before transitioning into the homogenous domains separated by thin resistive bands. There is no apparent change in lithology and the different signal is possibly related to cementation of the micritic limestone or potential fracturing. Sinusoidal geometry is highlighted with a dashed white line. (c) The FMI data from C3 display two conductive bed boundaries where the upper boundary is truncating the lower. See enlarged inserts 1 and 2. Below this, at c. 4094.2 m an inclined fabric can be observed within the domain confined by two conductive bands. We interpret these features to represent cross-stratification as can be observed in the enlarged area 3 with interpretation of the FMI data below. An impact of drilling artefacts cannot be fully ruled out. (d) The transition from a conductive domain into a thick, resistive homogenous domain. This corresponds to a lithological change from sandstone to carbonate. The top of this domain, at c 4078 m, shows that the resistive band comprises several thin discontinuous bands. Black arrows point towards a faint discordant fabric internally in the beds. (e) Thickness distribution of the carbonate beds derived from the FMI data. The thin red conductive lines define each layer's top and base as seen in the other subfigures. Each carbonate layer shows a thickening of the individual beds towards the top of the layer. The FMI data are too uncertain to estimate thicknesses from the carbonate part of C4.



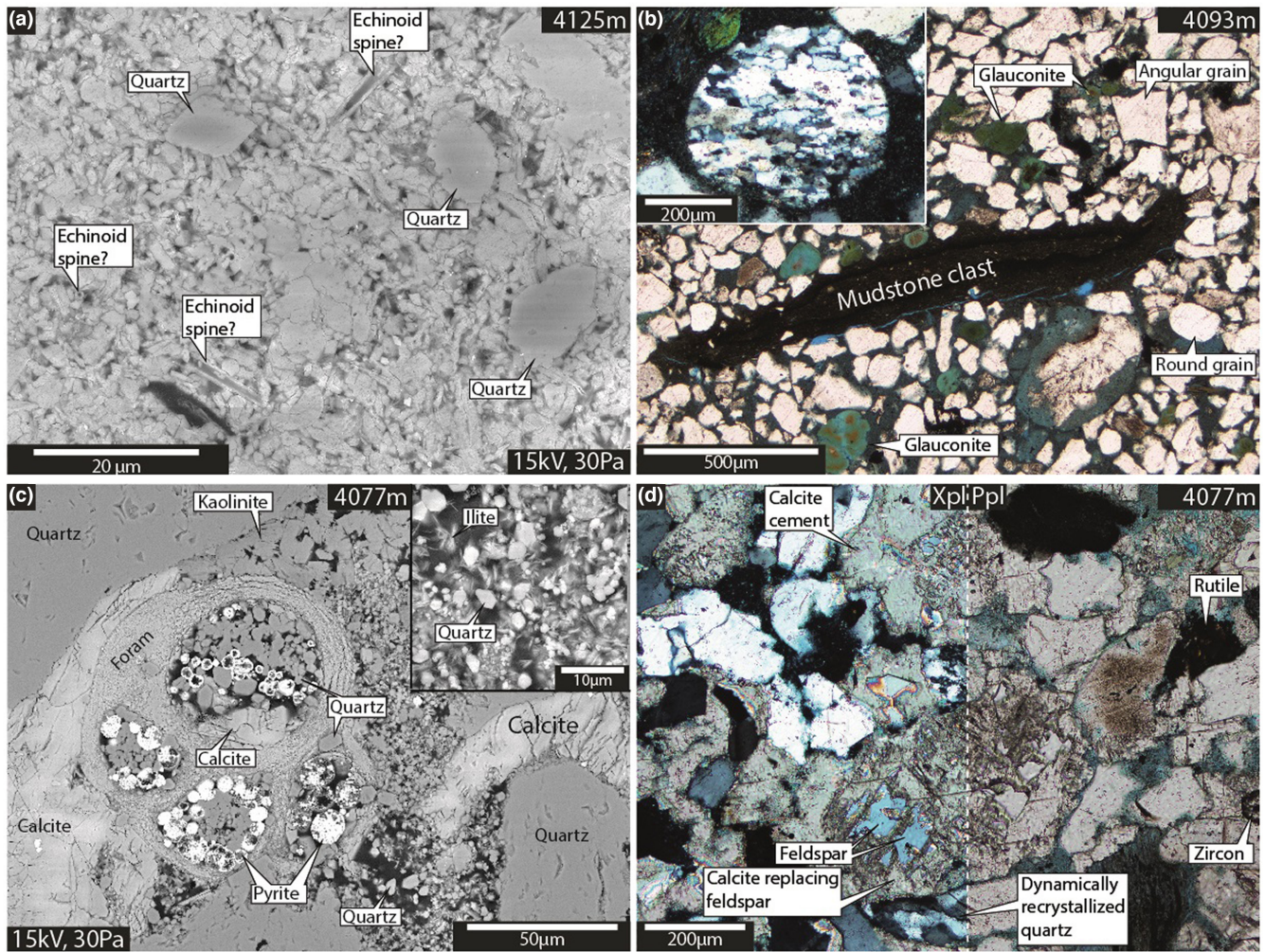


FIGURE 7 Photomicrographs from SWC from well 6302/6-1. (a) SEM BSE image of the very fine-grained micritic limestone. Some fossil fragments (echinoid spines, clay minerals and framboidal pyrite can be seen. Note that the carbonate is locally partially recrystallized. (b) Photomicrograph in plane polarized light of sandstone with a mudstone (Mst) rip-up clast. Inset shows a photomicrograph taken with crossed polarized light of a well-rounded and dynamically recrystallized quartz grain (i.e. metamorphic origin) from a different part of the same sample. (c) SEM BSE image of a filled foraminifera, the cement and siliciclastic grains and diagenetic products. Note the two-fold pore-space fill: (1) sparry calcite cement and (2) fine-grained quartz and possibly illite with intra-grain porosity. Insert show a zoom of the latter pore fill from a different part of the thin section. (d) Photomicrograph taken under crossed (left) and plane (right) polarized light. Note the dissolution of the feldspar grain, which has been filled with secondary calcite. Both zircon and rutile are present as well as dynamically recrystallized quartz.

upper part of Grisetang Member. They are, however, uncommon in the intervals that contain micritic limestone, although with some minor exceptions. Their rounded nature and similar size to the detrital quartz grains indicate that some transport prior to deposition was likely (e.g. Amorosi, 1997; Triplehorn, 1966). The sparse observations of craquelures (Figure 7b) could indicate that some glaucony production took place in situ as well or that these fragile features indeed did survive the transport (Amorosi, 1997).

Some of the SWC thin sections contain thin argillaceous horizons, these are generally interpreted to represent stylolites. Where the argillaceous horizons are thicker (cm-scale) and with a different fossil content

than what is observed for the stylolites, they are interpreted to represent hemipelagic background sedimentation during quiescence in the carbonate deposition. These thicker argillaceous horizons are likely to correspond to the thin conductive lines in the FMI and further substantiate the interpretation that these thin lines represent bed boundaries.

4.1.5 | Sautang Member

The Sautang Member is 76.3 m thick in the well (4074–3997.7 m). It has been sampled by 9 SWC that reveal a mixture of sandstone and mudstone.

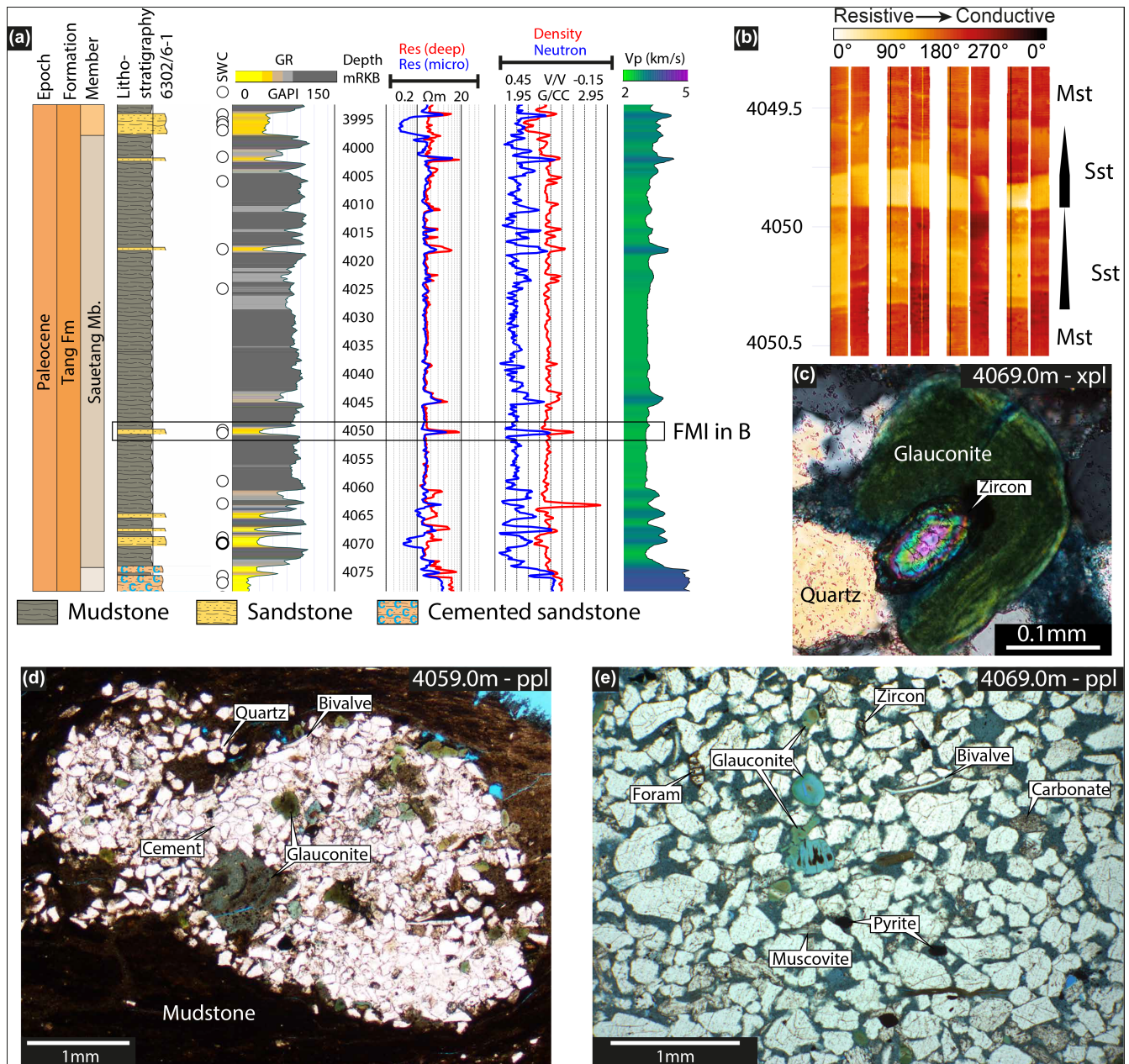


FIGURE 8 Overview of Sautetang Member. (a) Geophysical properties from the wireline log data. Spikes in gamma ray, resistivity, density and neutron can be seen where there are sandstones. In some cases, there is also an increase in V_p , where there are sandstones. This is usually due to carbonate cemented sandstones. (b) FMI of a 1 m section of the well where a 0.7 m thick sandstone layer occurs. The resistivity structure of the sandstone layer indicates that it is represented by two sandstone beds that appear to be normally graded, possibly indicating that it formed from a gravity flow. (c) Insert shows a zoned zircon wrapped in a glauconite pellet. Several of the samples contain euhedral zircon, but they have not been dated. (d) Pocket of cemented, fine-grained sand-siltstone in a mudstone. The abundances of glauconite and microfossil fragments are generally high in these distorted pockets. (e) Photomicrograph taken under plane polarized light displaying a poorly cemented sandstone primarily consisting of quartz and feldspar with a minor contribution from microfossils, mica and glauconite. The pore filling is similar to what is presented in Figure 7c.

A transition between the Sautetang Member and the Grisatang Member is found from 4047 to 4003 m. The wireline log responses are mainly characterized by high GR, low resistivity and a low V_p sonic response, consistent with their mudstone dominated nature (Table 2;

Figures 1 and 2). This monotonous pattern is locally interrupted by a distinct decrease in GR (from c. 80–100 to c. 36–38 GAPI), a slight decrease in density (from c. 2.4 to 2.3 g/cm³) and an increase in V_p (to c. 3.1 km/s), interpreted to represent sandy domains. These sand domains

are most frequent in the lowermost c. 14 m of the transition zone. The sandstone layers range in thickness from c. 0.5 to 1.6 m. The FMI images show disturbed beds indicating soft sediment deformation and locally extensive burrowing in the mudstones (Figure 8b). Locally, the mudstone displays a fine lamination (Figure 8b). A 1 m thick sandstone layer at 4050 m has an FMI signature that shows two stacked domains interpreted as beds. Both beds have a gradual decrease in resistivity towards the top. The boundary between the two beds is abrupt (Figure 8b).

Lithologically, the Sautang Member is dominated by mudstones and silty mudstones with minor sandstone layers, as constrained from the SWC and the geophysical well logs (Figure 8a). The sampled mudstones show that they are primarily composed of mud with some suspended silt-size, angular fragments of quartz and feldspar. Locally, small (<1 cm) pockets of siltstone are present (Figure 8d). These pockets often have rounded shapes, presumably caused by fluid escape during compaction and/or bioturbation. The pockets contain a higher abundance of mica, glauconite and microfossils.

The sandstone layers in the Sautang Member are similar to those found in the Sagtang- and Grisatang members. They are composed of quartz, feldspar, lithic fragments as well as carbonate clasts all of which are variably rounded and generally with a bimodal grain size distribution (Figure 8e). Some of the sandstones show a matrix consisting of argillaceous mud, and these are generally mud-supported. Plagioclase feldspar grains often show partial dissolution and partial replacement by carbonate. Accessory minerals include rounded glauconite pellets, detrital muscovite flakes, rutile, zircon, and microfossils (Figure 8e). The cement varies from only minor carbonate (likely calcite) cement, to completely cemented sparry carbonate. Locally, fine-grained (<5 μm) quartz and clay minerals (perhaps illite) are present similar to what can be observed in Figure 7c.

4.1.6 | Interpretation of the data from the Sautang Member

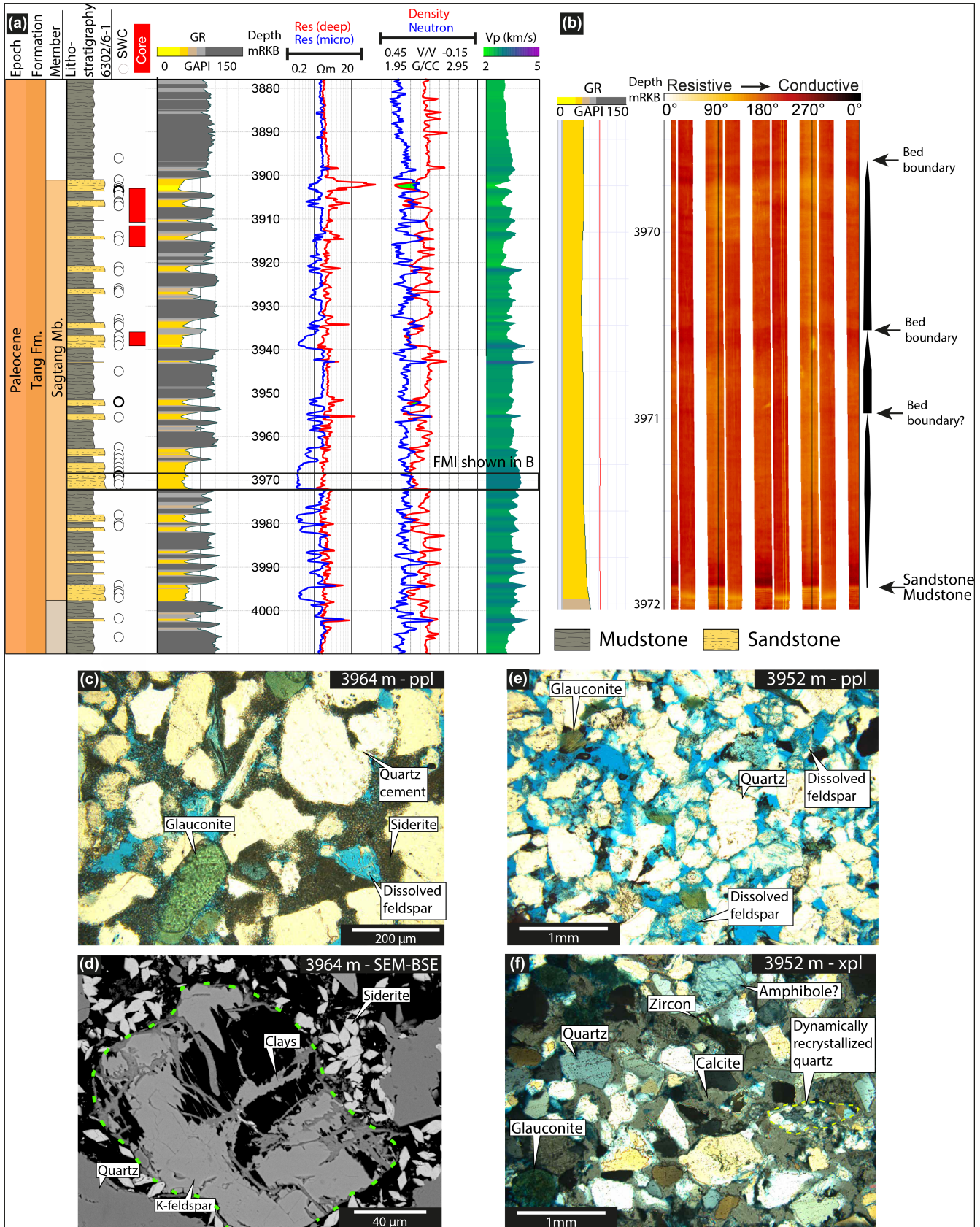
The FMI data show trends that are similar to upwards fining sequences with sharp transitions to new sequences in some of the sand layers, indicating that these are stacked sandstone beds with increasing mud content towards the top of the individual beds, i.e. they show a normal grading, suggesting that they deposited by a gravity flow (e.g. Talling et al., 2012). The type and shape of glauconite is consistent with an allochthonous origin and it is further corroborated by the presence of detrital muscovite grains. Where the mudstone samples are homogenized by bioturbation it is indicated that the sediment was deposited in an oxygenated bottom-water environment with low sedimentation rate (e.g. Boulesteix et al., 2019).

4.1.7 | Sagtang Member

The Sagtang Member measures 96.3 m in the well (3997.7–3901 m) and is sampled by 30 SWC (Figures 1, 2 and 9). It is composed of two primary lithologies: mudstone and sandstone where the mudstone dominates and the sandstone occurs as evenly distributed beds throughout the member. The sandstone layers range in thickness from >10 cm to c. 7 m (Table 2; Figure 9).

From the wireline logs, it is calculated that the upper Sagtang Member contains c. 20% sand-dominated lithologies and 80% mud-dominated lithologies (Figure 9a). The sandstone layers have an average thickness of c. 1.1 m with a range from 0.2 to 4.7 m in thickness (Table 2). Their GR signal averages at 46.5 ± 1.5 GAPI and average neutron porosity of 0.25 ± 0.02 (Table 2). The average V_p is 2.97 ± 0.05 km/s (Table 2). The same pattern can be observed for the density where the two uppermost sandstone units have an average density of 2.23 ± 0.08 g/cm³, whereas the rest of the sandstone layers have densities of 2.35 ± 0.03 g/cm³. The mudstones on the other hand have

FIGURE 9 Overview of the Sagtang Member. (a) Wireline logs from well 6302/6-1. Note the characteristic pattern of the sandstones with low Gamma ray, low resistivity, and decrease in density, especially where the sands are charged with hydrocarbons (yellow area on the neutron, density graph). (b) GR and FMI log that shows stacked sandstone beds. Arrows point towards conductive bed boundaries, presumably more clay-rich and black bars indicate mud content. (c) Photomicrograph taken under plane polarized light of sandstone with rounded glauconite pellets and angular grains, primarily quartz. The sample is partially cemented by euhedral siderite rhombs and shows some indications for quartz dissolution-precipitation at quartz grain contacts. (d) SEM-BSE image from the same sample as in c. The image shows a partly dissolved K-feldspar grain with some mixed clays present inside the dissolved grain, whereas siderite rhombs are only present outside the dissolved grain (yellow dashed line). (e) Photomicrographs taken with plane polarized light of sandstone with glauconite, quartz grains and dissolved feldspars. The blue in the photograph is open porosity. The photomicrograph shows very little cement. (f) Photomicrograph with crossed polarized light shows the same sample as in F, but in this part of the thin section the sample is completely cemented by sparry calcite. Note the diversity of grains, including possibly an amphibole grain and dynamically recrystallized quartz, highlighted by a yellow dashed line.



an average GR of 77.4 ± 14.0 GAPI, neutron porosity of 0.30 ± 0.03 and V_p of 2.84 ± 0.08 km/s. The FMI logs cover most of the Sagtang Member, but above 3910.7 m, the data

are not available. Some of the sandstone layers represent multiple stacked beds that show thin (c. 20 cm) conductive bands separating more resistive domains. Some of the

resistive domains show a gradual change in conductivity towards the conductive bands (Figure 9b).

The sandstone layers in the Sagtang Member consist of fine to medium-grained sandstones with grains of quartz, feldspar and some lithic fragments with minor amounts of microfossils (Figure 9c–f). The feldspars are generally almost completely dissolved, and it varies whether the voids are filled with clays, sparry calcite cement or open voids (Figure 9d,e). Some dissolution and precipitation of quartz can be observed between neighboring quartz grains but is minor (<5%; Figure 9c). Rounded glauconite pellets are common (Figure 9c,e,f). The cement varies between sparry calcite and euhedral siderite rhombs (Figure 9c,d,f). The degree of cementation varies with some samples displaying very little cement (ca <5%), while some are completely cemented (Figure 9c–f). Mudstone rip-up clasts are observed in some of the thin sections. The mudstone layers are locally sampled by the SWC and show similar characteristics as the mudstone layers in the Grisetang and Sauetang members. The silt-sized grains occur both as grain-supported pockets and/or as more distributed silty mudstones. The grains are primarily composed of quartz and feldspar with some muscovite flakes with fringed edges. Fossils, such as calcispheres, bivalve fragments and radiolarian as well as rounded glauconite pellets, are abundant.

4.1.8 | Interpretation of the data from the Sagtang Member

The pattern observed in the FMI data suggests that the sandstone beds in the Sagtang Member show an internal normal grading. This together with the presence of rounded glauconite pellets and mudstone rip-up clasts suggests an allochthonous origin of the sandstone beds. The grain size of the sandstone and the lack of mud indicate that the sand was deposited from gravity flows, such as turbidite flows (Talling et al., 2012). The source area of the sands included metamorphic terrane or sandstone that had previously sampled a metamorphic terrane as seen from the presence of dynamically recrystallized quartz. The partial calcite cementation indicates that the concentration of dissolved calcite was too low to completely cement the sample and that the samples likely represent distributed concretions (Bjørkum & Walderhaug, 1990; Dutton et al., 2002).

4.2 | Seismic interpretation

A total of four horizons were picked using guided autotracker where possible and manual picking where necessary (Table 4). The horizons have not been picked below volcanics because of the low confidence.

TABLE 4 Seismic characteristics and confidence in interpretation for the picked horizons.

Horizon	Seismic character	Confidence
Top Tang Fm.	High amplitude, hard reflection	High
Top Sagtang Mb.	High amplitude where gas-charged and moderate amplitude elsewhere. Generally soft reflection	High in the west, low in the east
Top Grisetang Mb.	High to moderate amplitude, hard reflection.	High in the west, low in the east
BPU (Base Grisetang Mb.)	High amplitude and soft where Grisetang Mb. is present. Low amplitude, to the east	High where overlain by Grisetang, moderate to low elsewhere

4.2.1 | Seismic expression of the Base Paleogene Unconformity (BPU)

The Base Paleogene Unconformity, also marking the base Tang Formation, is present across the entire 3D cube, but is locally masked by lavas and shallow intrusions in the south and western parts. The BPU is generally present as a broad, coherent and continuous, high amplitude, soft reflection caused by the lithological change from carbonate to mudstone (Figure 3), in contrast to other parts of the Norwegian Sea where it is characterized as a clear hard reflection within siliciclastic strata (e.g. Zastrozhnov et al., 2020). In the eastern part of the cube, however, the BPU is diffuse, semi-coherent and challenging to follow with high confidence (Figure 10).

Internally, the Springar Formation is homogenous (Figures 2 and 11). It can be followed down to an underlying saucer-shaped Tulipan Sill (e.g. Kjoberg et al., 2017; Schmiedel et al., 2017), without any high amplitude reflections (Figure 2). The succession displays semi-coherent, low amplitude reflections, which brighten towards the top of the sill, potentially related to gas. East of the Tulipan Sill area, the Cretaceous succession is weakly reflective, and is offset by numerous small-offset normal faults (Figure 10).

4.2.2 | Grisetang Member seismic expression

The top of the Grisetang Member corresponds to a coherent, medium amplitude, hard reflection that can be traced eastward to where it converges with the BPU (Figure 10).

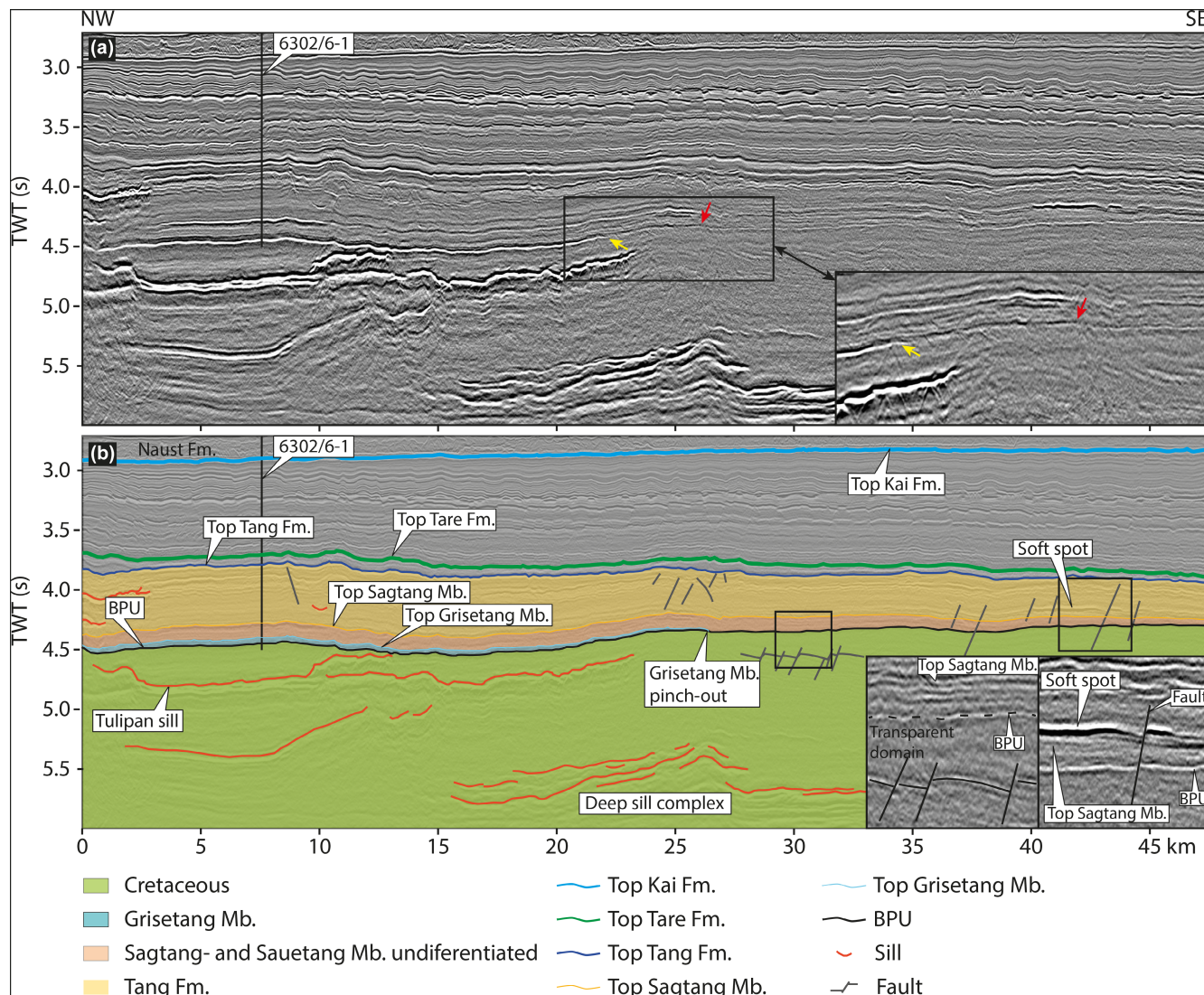


FIGURE 10 Overview of a key seismic cross section. (a) Uninterpreted seismic cross section. Red arrow shows the approximate extent of the Grisetang Member in this seismic section and the decrease in amplitude for the BPU is shown by the yellow arrow. See insert for details (b) Interpreted seismic section. Note the thinning of the Tang Formation and all of its members towards the southeast. Inserts show rotated reflections in the Upper Cretaceous overlain by a seismically transparent domain below the BPU. The BPU is locally cut by normal faults, which also delineate a soft spot just above the top Sagtang reflection. Also note the very subdued reflection of the Top Sagtang reflection where it is not gas-charged. Sautang Member is located between Sagtang and Grisetang Member. The sills interpreted in the seismic section are volcanic intrusions related to the break-up of the NE Atlantic in the Eocene.

Above the Tulipan sill, the Grisetang Member is sufficiently thick to resolve some discordant and concordant internal reflections, with respect to the base and top of the member (Figure 2), however, as the Grisetang Member thins towards the east, internal details are unresolvable. Around 20 km to the east-southeast of the Tulipan well, the Grisetang Member thins to below seismic resolution and is not mappable. The western and southern continuation of the carbonate layer is obstructed by numerous intrusions and can only locally be mapped.

4.2.3 | Sautang Member seismic expression

Top Sautang Member has not been confidently mapped in the 3D cube, due to too subtle lithological features that are unresolvable by the seismic cube at hand (Figures 2 and 10). Internally, the Sautang Member has a weakly reflected signature without any strong reflections, except for the base, which is the top of the carbonates and displays a hard reflection caused by the positive change in impedance (Figures 2 and 10).

4.2.4 | Sagtang Member Seismic expression

The top Sagtang Member is mappable in most of the seismic 3D volume, mainly as a coherent, medium amplitude, soft reflection, but the amplitude changes significantly throughout the volume (e.g. Figure 10). Above the Tulipan sill, the reflection is a high-amplitude reflection that corresponds to the gas-charged reservoir at the Tulipan well, which is hosted by the topmost layers of the Sagtang Member. Like the other horizons, it is masked by volcanics to the west but is traceable eastwards. The Sagtang Member thins towards the east, and downlaps onto the BPU c. 45 km east of the Tulipan well.

A gentle high, c. 34 km east of the well the top Sagtang Member reflection becomes a high amplitude, soft

reflection. In map view, these high amplitude domains are cut by numerous normal faults (Figure 11). Given the similarities in amplitude with the Tulipan discovery, it is possible that some of these high amplitude domains also represent gas-charged sandstones, and thus represent several small (accumulated 27 km²) gas pockets with structural and/or stratigraphic traps (Figures 10b and 11).

4.2.5 | Seismic expression of the Top Tang Formation

The top of the Tang Formation corresponds to a high-amplitude hard reflection that can be traced with good confidence throughout the seismic cube. The topmost c. 150ms of the

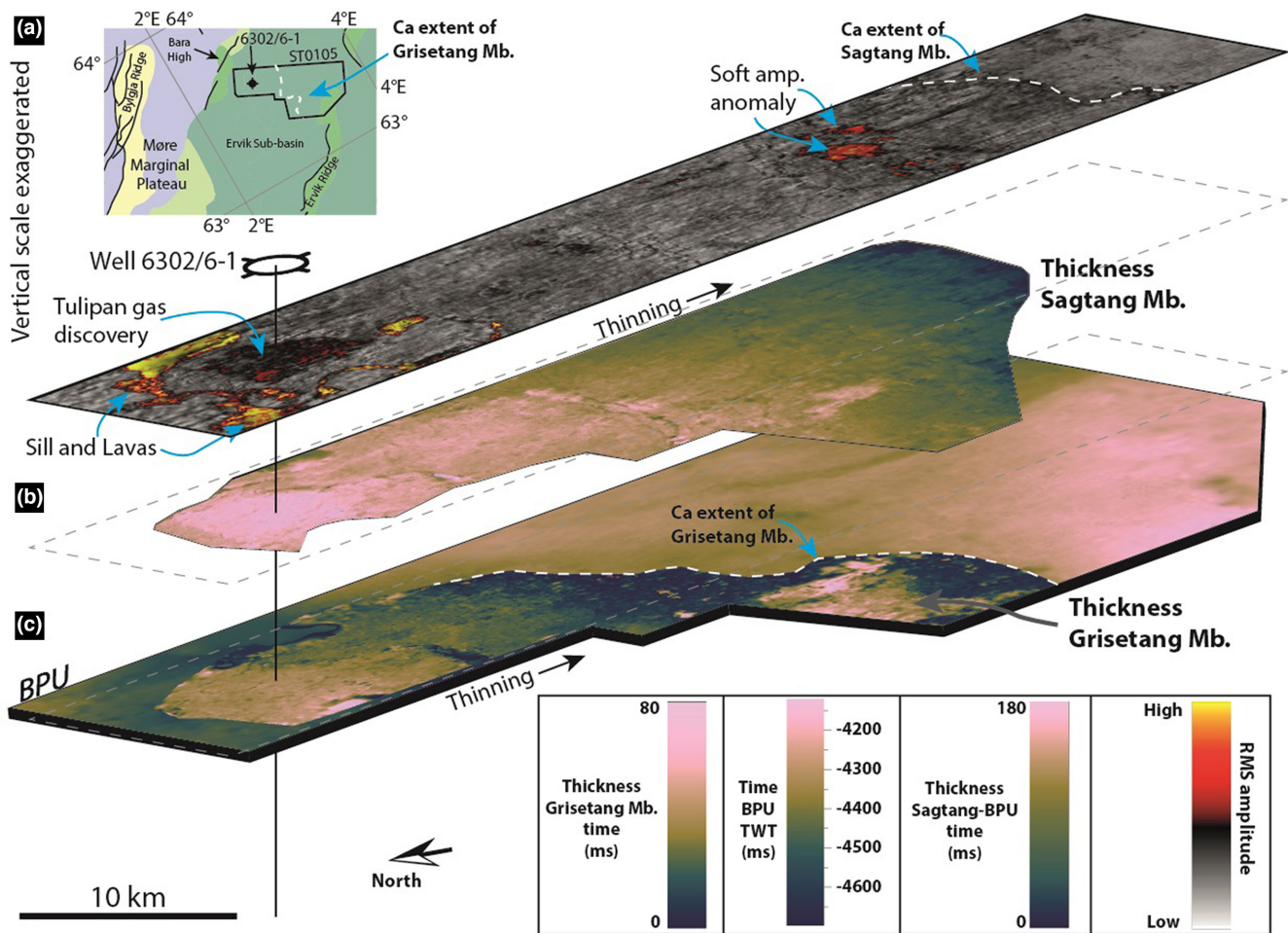


FIGURE 11 Oblique view of thickness maps and an attribute map of top Sagtang Member. (a) RMS map of the top Sagtang Member (+60 ms above and 5 ms below) shows clearly where the transgressive sides of the Tulipan Sill penetrate the BPU (Yellow—very high variance). The Tulipan gas discovery can also be seen as a high variance (red and black) domain surrounding the Tulipan well. Similarly, we can see the small, soft amplitude anomaly in the south eastern part of the cube. (b) Thickness map between the top of the Sagtang Member and the BPU. Note thinning towards the right (southeast). (c) Thickness map of the Grisetang Member above the BPU topography in time. It shows that the Grisetang member thins towards the southeast but also that there are some internal thickness variations. Stippled line in b and c shows the extent of the map in a. Inserted map shows the study area and the c. extent of the Grisetang Member as mapped out by the seismic interpretation. The figure is not to scale in the vertical dimension.

Tang Formation is characterized by several high-amplitude events that are locally affected by extensional faults. The reflections in this domain are generally semi-continuous, and not parallel to the top horizon everywhere (Figure 10), forming shallow depositional basins between local highs. This is the unit with hydrothermal vents as described in Kjøberg et al. (2017). Below this uppermost domain and above the Sagtang Member, the Tang Formation is transparent with only some amplitude variations. The entire Tang Formation thins from c. 800 to c. 300 m towards the southeast (Figure 10).

5 | DISCUSSION

5.1 | Depositional model

The stratigraphic information in the dataset in context with a regional understanding allows a first-order reconstruction of basin development and sedimentary response. The stratigraphic units and the major boundaries in the succession are discussed in chronological order.

The open marine Cretaceous Springar Formation in the Norwegian Sea episodically received sediment turbidite flows from the basin edges (e.g. Dalland et al., 1988; Southern et al., 2017). This is corroborated by SWC samples, containing silty mudstones with abundant angular to sub-angular silt-sized quartz and feldspar grains, as well as detrital mica and rounded glauconite pellets with a similar size range as the detrital grains (Figure 4). This suggests that gravity flow systems were active as early as the Late Cretaceous and that their distal parts, including the waning mud plumes, reached the study area.

The Base Paleogene Unconformity (BPU) represents the basin floor for the uppermost Cretaceous to Lower Palaeocene succession (Figure 2) and marks the onset of compositionally mixed carbonate-siliciclastic deposition in the area (sensu Chiarella et al., 2017). The biostratigraphic report from the Tulipan well suggests that the BPU does not represent a significant hiatus (Mahdi & Ayress, 2006), rather, it is either a short depositional hiatus and/or a shift in tectonic style/environment that led to a margin-wide change in the rifting style as described for the FSB (Booth et al., 1993; Goodchild et al., 1999; Lamers & Carmichael, 1999). The change from pure siliciclastic detritus in a distal turbidite system below the BPU to deposition of compositionally mixed carbonate and siliciclastic deposits occurs at the BPU, thus marking a significant change in the basin fill history.

5.1.1 | Depositional model for the Grisetang Member

The compositional- and strata-mixed Grisetang Member (sensu Chiarella et al., 2017) has a vertical transition

where the base of C1 comprises a mixed carbonate siliciclastic packstone, which grades into a laminated packstone with little (<10%) siliciclastic material. However, the entire Member shows strata mixing with alternating bed-sets of carbonate dominated material (micritic limestone) interlayered by siliciclastic mudstones (Figure 4). Such stratigraphic mixing of carbonate and siliciclastic bed-sets is common in distal portions of fine-grained calciclastic basin floor strata as the deposit grades into the basinal deposits (e.g. Payros & Pujalte, 2008). The location of the Tulipan well with respect to the depositional complex is corroborated by the seismic analyses, which clearly show the Grisetang Member pinch-out and downlap towards the east, onto the BPU, c. 45 km east of the well (Figure 11). Because of the lack of siliciclastic mud in the fine-grained, allochthonous micritic deposits, it is generally agreed that such detritus can be transported large distances onto the basin floor and form unconfined sheets intercalated with hemipelagics (Loucks et al., 2011; Payros & Pujalte, 2008). For the Grisetang Member, this is observable due to the impedance contrast between dense carbonate above underlying mudstones of the Springar Formation, resulting in a strong negative, soft reflection (Figure 2), in contrast to the regional description of the BPU by e.g. Zastozhnov et al. (2020), highlighting the local nature of the carbonate deposit. Where the Grisetang Member pinches out to below seismic resolution, the BPU reflection becomes weak and mottled (Figure 10) due to juxtaposition of mudstone in the Springar Formation below primarily mudstones in the Sautang- and Sagtang members.

The wide (>30 km) depositional front with a lobate shape, together with the thickening of the sediment wedge towards the west suggests that the carbonate material likely originated from a line source, originating to the west of the study area (Figures 10 and 11). This is corroborated by the distinct lack of observable channels or lobes, which is a common feature in very fine-grained carbonate apron deposits. The relatively flat base of the deposit and its distance from the nearest structural high suggests that it is not a base-of-slope apron, but rather a basin-floor apron with some similarities to the fine-grained calciclastic seafloor-fans as described by Payros and Pujalte (2008).

The thickening upward pattern observed in the Grisetang Member wireline data together with the observations of thin mudstone veneers and thicker mudstone deposits deposited between the carbonate layers (Figure 6c,e) is interpreted to represent the internal architecture of the apron (Figure 12). Because the source area is masked by significant extrusive and intrusive volcanic products, it is challenging to constrain the nature of the carbonate-producing system, but the interlayering of hemipelagic mudstones and the very fine-grained, laminated micritic limestone suggest that the sampled

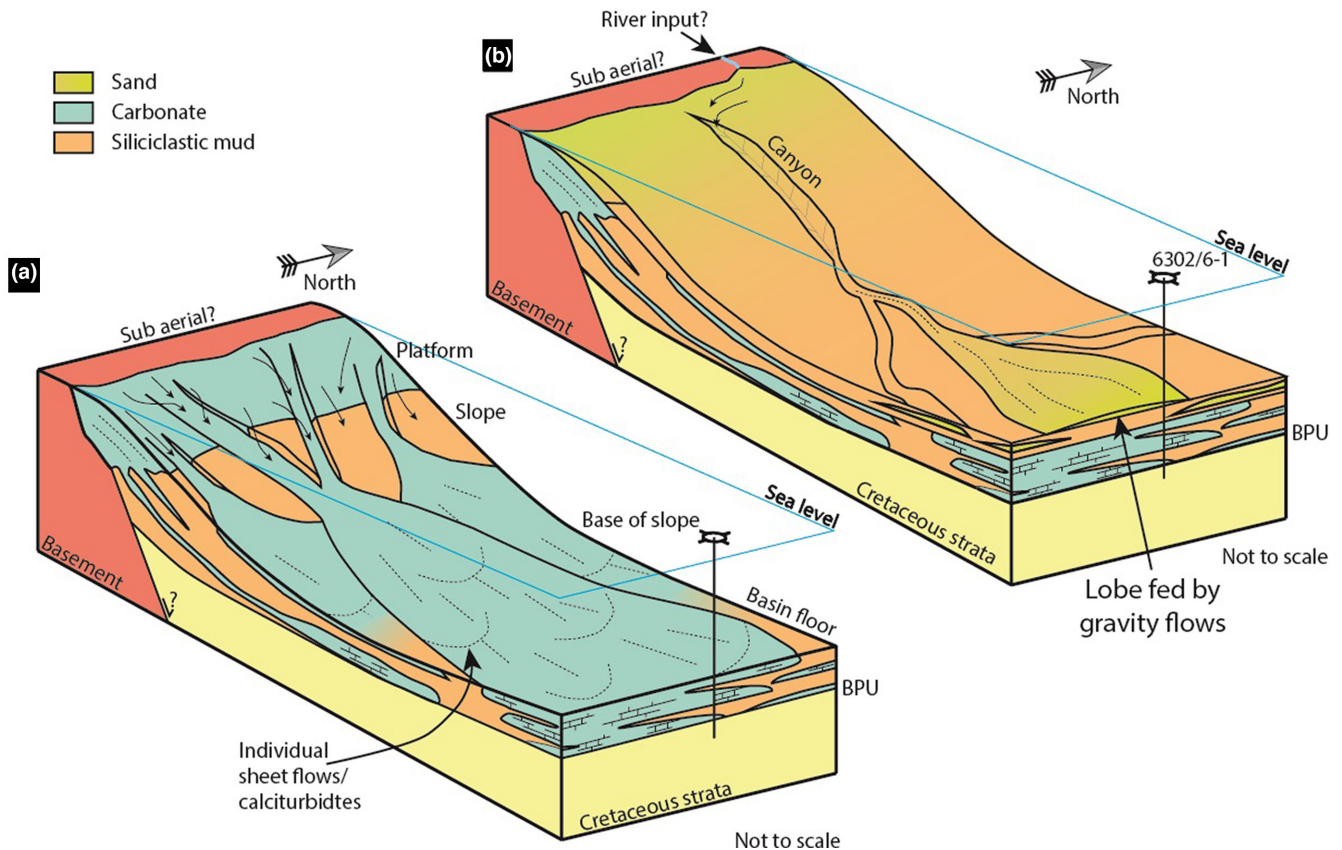


FIGURE 12 Simplified Tulipan depositional model based on concept from Payros and Pujalte (2008) and Mullins and Cook (1986). (a) Depicts a carbonate apron where the allodapic sediment is partly channelized in numerous shallow canyons and runs out onto the basin floor, primarily as calciturbidites. Hemipelagic material is constantly deposited on the basin floor and covers non-active parts of the apron. The input of sandy material could stem from, e.g., sub-aerial erosion of a basement complex to the west. (b) After deposition of the Grisatang Member the system becomes a pure siliciclastic system, and point-sourced sand is deposited in a basin-floor fan by gravity flows.

stratigraphy is in the seaward fringe of the apron (Loucks et al., 2011; Mullins & Cook, 1986; Payros & Pujalte, 2008; Playton et al., 2011). Sømme et al. (2019) report a peak in relative sea level for the Northern North Sea during the Maastrichtian and Danian which presumably would also affect the Møre Basin and surrounding structural elements, leaving the possibility that the described carbonates are a result of highstand shedding from a nearby high (e.g. Loucks et al., 2011; Schlager et al., 1994).

Contributions from hypopycnal flows and wind-borne hemipelagic dust may have contributed to the minor clay content within the micritic limestone and the hemipelagic mudstones between the carbonate beds, however, it is the lack of mud within the carbonates that appears to be the most important feature. Carbonate drifts are deemed unlikely to have contributed significantly to the deposition of the micritic limestone in the Grisatang Member, primarily because we do not see any evidence for contourite drift deposits in the seismic data, such as sediment waves, along with the dominant lack of mixing with siliciclastic material (e.g. Anderskov et al., 2010; Eberli & Betzler, 2019). A more local influence from

bottom currents, such as reworking of the turbidite deposits (Faugères & Mulder, 2011; Rebesco et al., 2014) or of the hemipelagic suspension fall-out appears more likely. The Early Palaeocene increasingly warmer and wetter climate (Stokke et al., 2021 and references within) is likely to have caused elevated weathering and runoff rates in the sediment source areas (e.g. Sømme et al., 2019). This would have enhanced the terrigenous extrabasinal sediment supply and may have blanketed and shut off the carbonate factory that fed the Grisatang Member and thus caused the transition into a pure siliciclastic system.

5.1.2 | Depositional model for the Sautang and Sagtang Members

Sand and silt is common throughout the Sautang Member, but the abundance increase during deposition of Sagtang Member. A wide depositional front is also observed for the Sautang and Sagtang Members, similar to that of the Grisatang Member. Line sourced

apron-type deposits for pure siliciclastic material are, however, generally related to very coarse and proximal deposits (Ravnås et al., 2000; Ravnås & Steel, 1997; Ravnås & Steel, 1998), in contrast to the strata studied here. We, therefore, propose that they belong to a point sourced fan, fed from the west (Figures 11 and 12b). The absence of discernible channel features in the seismic data suggests a distal fan setting. Alternatively, the primary transport features, such as channels and levees, are flattened/smoothed out by secondary processes in the basin such as contourite currents (e.g. de Castro et al., 2020; Fonnesu et al., 2020; Moraes et al., 2007; Rebesco et al., 2014). Recent studies of structural highs fringing coastal environments from 3D seismic data in the Faroe-Shetland basin to the south have documented multiple strand-plane type coastal deposits associated with channel incision systems within the Palaeocene to Eocene (Walker et al., 2022). However, to date, imaging of the slope and extent of the coastal transition to the west of our study areas remains complicated by the impact of later volcanic rocks on seismic imaging.

5.2 | Sediment sources

The velocity, GR, and resistivity for the carbonate and siliciclastic sandstones in the Grisatang Member are rather similar, therefore the actual boundary can be challenging to pick from the wireline data alone. However, by utilizing the FMI data the boundaries between the carbonate and sandstone appear to be conformable. These two lithologies, in such close stratigraphic proximity, suggest strongly contrasting sediment sources. The sandstone, with its low GR signal and some indications for formation of cross-beds (10–20 cm-scale; Figure 6a,c), further suggests that these lithologies are allochthonous, i.e. have been transported into the deeper part of the basin and presumably derived from a clay-poor proximal source and then remobilized and deposited on the basin floor. Alternatively, the mud component was removed by hydrodynamic processes during transport (e.g., Talling et al., 2012).

Based on the mineralogy of the sand grains, it is likely that the sand fraction is sourced from two different sources; one either with metamorphic rocks or already reworked metamorphic rocks (dynamically recrystallized quartz) and one with a possible magmatic origin (non-recrystallized quartz, euhedral zircons, K-feldspar and plagioclase). Furthermore, there are also two fractions of size and rounding of the grains (Figure 7). The rounding suggests some transport prior to deposition, or that they are reworked sedimentary rocks, whereas the more angular silt-sized grains experienced shorter transport. This implies at least two sources for the siliciclastic

sand grains, where one involves metamorphic basement. The source area is challenging to constrain, but metamorphic basement rocks were likely exposed on Greenland and Norway during the time of deposition (Fonneland et al., 2004; Martinsen et al., 2005). Due to the shape of the deposit as constrained from the seismic interpretation in this contribution as well as the basin topography at the time, we deem it unlikely that either the carbonate or the sands were sourced directly from the east, i.e., mainland Norway. Heavy mineral analysis will enable greater insights into sand sourcing in future studies.

The interlayered mudstone that separates the C1-C4 carbonate layers in the Grisatang Member and the sandstone beds in Sautang- and Sautang-Member, generally contain silt-sized detrital grains as well as microfossil particles (Figure 7). Consequently, no carbonate material or sand reached the sampled well area during these times. One reason could be avulsion at the apex such that the material was transported elsewhere on the apron and fan and that the silty mudstones represent the background sedimentation in the basin (e.g., Picot et al., 2016). Alternatively, they could indicate changes in relative sea level, which is known to influence both carbonate production and allodapic shedding (e.g., Handford & Loucks, 1993; Reijmer et al., 2015).

Sediment source areas would be a local structural high, such as the Bara High or the more extensive Bylgja Ridge, a part of the Møre Marginal Plateau (Figure 1). Alternatively, the larger Jan Mayen Block, which was located outboard of the study area and connected the Møre Basin with Greenland prior to break-up (Figure 1) could be the source of the sandstone beds in the Sautang and Sautang Member as these areas have Proterozoic-Archean basement rocks (Polteau et al., 2019; Theissen-Krah et al., 2017). The distance from the Bylgja Ridge (Figure 1) to the Tulipan well today is roughly 130 km, a distance which is within range for fine-grained calciturbiditic flows (e.g. Amy & Talling, 2006; Andresen et al., 2003; Dade & Huppert, 1994; Talling et al., 2012). Distinguishing these candidates is, however, challenging as they were all part of the same terrane prior to break-up.

A recent IODP cruise (Expedition 396; Planke et al., 2022) revealed that a similar structural high at the Vøring Margin (the Kolga High; Figure 1) is composed of weathered granite and flanked by sub-aerial basalt, indicating that the high was exposed above sea level at the time of the basaltic eruptions likely in the Eocene (Planke et al., 2022). Such a weathered granite could have sourced the sandstones studied here but whether it was exposed during the time of sediment shedding is unclear. Seismic evidence for the Bara and Bylgja High,

are, however, somewhat poor due to the challenges of sub-basalt seismic imaging. They have nevertheless been mapped in some detail (Zastrozhnov et al., 2020). Significant topographic variations mapped within the volcanic-covered areas to the west of Tulipan reveal potential pathways for sediments to enter the Møre Basin from the west prior to continental breakup (Millett et al., 2022).

The nearest known chalk is in the Northern North Sea, to the south of the Møre Basin (Figure 1). Although it is within plausible distance for gravitational flows to reach the study area, the paleo-bathymetry of the Møre Basin, with elements such as the Ervik High, would likely restrict sediments from reaching the Tulipan area. It is more likely that there was a carbonate source somewhere to the west of the Tulipan area and Polteau et al. (2019) do indeed report finding carbonate rocks from a dredge sample from the Jan Mayen escarpment. They do, however, not report an age of the carbonate, nor its composition. The presence of the micritic limestone of Late Cretaceous to Early Palaeocene age in the central part of the Møre Basin suggests that the chalk province of the North Sea could be extended several 100 km to the north from its current location. It should be emphasized, however, that there is not necessarily a lateral continuity between the Chalk Group in the Northern North Sea and the micritic limestone described herein.

6 | CONCLUSIONS

- During the Late Maastrichtian, the Møre Basin transitioned from siliciclastic- to carbonate-dominated across the Base Paleogene Unconformity (BPU).
- This is the first detailed description of Chalk Group-type sediments in the Møre Basin and thus extends the Late Cretaceous-Early Palaeocene Chalk Group several 100 km north from previous studies.
- Directly above the Base Paleogene Unconformity (Grisetang Member), a basin-floor carbonate apron formed by carbonate sheet flows and calciclastic turbidites developed. It was composed of fine-grained remobilized mixed carbonate and siliciclastic detritus, chalk and siliciclastic sand.
- The carbonate apron was abruptly replaced by a siliciclastic, mud-dominated (Sautang Member) and sand-rich fan (Sagtang Member) in the Early Palaeocene.
- The carbonate sediment was formed in shallow water, fringing structural highs before remobilization into the deep basin.
- The siliciclastic sediments were westward sourced, from the Møre Marginal Plateau or sediment pathways crossing it from Jan Mayen and/or East Greenland.

ACKNOWLEDGEMENTS

This study was funded by Aker BP through the project “80-40 Palaeocene”. We thank Equinor for providing thin sections and petrophysical and geological well reports from the Tulipan well. SLB is acknowledged for providing the free academic licence for the seismic software Petrel. This manuscript benefitted from two thorough reviews by Domenico Chiarella and Aurélia Privat as well as additional comments and swift editorial handling by associate editor Craig Magee. Henrik Svensen is thanked for providing some of the microphotographs and SEM images. Wolfram Kürschner, Jenő Nagy, Jens Jahren are thanked for discussions regarding the microfossil assemblage and diagenetic history of the samples. Thea Hatlen Heimdal is thanked for her support and for reading an early version of the manuscript. HJK acknowledges the contribution of Synnøve and Alfred, without whom this manuscript would have been done a year earlier.

CONFLICT OF INTEREST STATEMENT

There are no conflicts of interest.

DATA AVAILABILITY STATEMENT

The 3D seismic data (ST0103) and well data that support the findings of this manuscript are released and available through DISKOS at <https://www.npd.no/en/diskos/>, the Norwegian National Data Repository for Petroleum data. Thin sections are the property of Equinor SA.

ORCID

Hans Jørgen Kjøll  <https://orcid.org/0000-0001-9560-3389>

Ivar Midtkandal  <https://orcid.org/0000-0002-4507-288X>

Sverre Planke  <https://orcid.org/0000-0001-6128-2193>

John Millett  <https://orcid.org/0000-0002-1275-6206>

Ben Manton  <https://orcid.org/0000-0002-0692-2706>

Kresten Anderskouv  <https://orcid.org/0000-0002-6853-9737>

REFERENCES

- Amorosi, A. (1997). Detecting compositional, spatial, and temporal attributes of glaucony: A tool for provenance research. *Sedimentary Geology*, 109(1), 135–153.
- Amy, L. A., & Talling, P. J. (2006). Anatomy of turbidites and linked debrites based on long distance (120×30 km) bed correlation, Marnoso Arenacea Formation, Northern Apennines, Italy. *Sedimentology*, 53(1), 161–212.
- Anderskouv, K., & Surlyk, F. (2011). Upper Cretaceous chalk facies and depositional history recorded in the Mona-1 core, Mona Ridge, Danish North Sea. *GEUS Bulletin*, 25, 1–60.
- Anderskouv, K., Surlyk, F., Huuse, M., Lykke-Andersen, H., Bjerager, M., & Tang, C. (2010). Sediment waves with a biogenic twist

- in Pleistocene cool water carbonates, Great Australian Bight. *Marine Geology*, 278(1–4), 122–139.
- Andresen, N., Reijmer, J. J., & Droxler, A. (2003). Timing and distribution of calciturbidites around a deeply submerged carbonate platform in a seismically active setting (Pedro Bank, Northern Nicaragua Rise, Caribbean Sea). *International Journal of Earth Sciences*, 92(4), 573–592.
- Bjørkum, P. A., & Walderhaug, O. (1990). Geometrical arrangement of calcite cementation within shallow marine sandstones. *Earth-Science Reviews*, 29(1–4), 145–161.
- Blystad, P., Brekke, H., Færseth, R. B., Larsen, B. T., Skogseid, J., & Tørudbakken, B. (1995). Structural elements of the Norwegian continental shelf: The Norwegian Sea region, Stavanger. *The Norwegian Petroleum Directorate, NP-D-Bulletin (trykt utg.)*, 8, 1–64.
- Booth, J., Swiecicki, T., & Wilcockson, P. (1993). The tectono-stratigraphy of the Solan Basin, west of Shetland. In *Proceedings Geological Society, London, Petroleum Geology Conference Series* (Vol. 4, pp. 987–998). Geological Society of London.
- Boulestex, K., Poyatos-Moré, M., Flint, S. S., Taylor, K. G., Hodgson, D. M., & Hasiotis, S. T. (2019). Transport and deposition of mud in deep-water environments: Processes and stratigraphic implications. *Sedimentology*, 66(7), 2894–2925.
- Brekke, H. (2000). The tectonic evolution of the Norwegian Sea Continental Margin with emphasis on the Vøring and Møre Basins. *Geological Society, London, Special Publications*, 167(1), 327–378.
- Chiarella, D., Longhitano, S. G., & Tropeano, M. (2017). Types of mixing and heterogeneities in siliciclastic-carbonate sediments. *Marine and Petroleum Geology*, 88, 617–627.
- Dade, W. B., & Huppert, H. E. (1994). Predicting the geometry of channelized deep-sea turbidites. *Geology*, 22(7), 645–648.
- Dalland, A., Worsley, D., & Ofstad, K. (1988). A lithostratigraphic scheme for the Mesozoic and Cenozoic succession offshore mid-and northern Norway. *NP-D Bulletin*, 4, 1–65.
- Damholt, T., & Surlyk, F. (2004). Laminated–bioturbated cycles in Maastrichtian chalk of the North Sea: Oxygenation fluctuations within the Milankovitch frequency band. *Sedimentology*, 51(6), 1323–1342.
- de Castro, S., Hernández-Molina, F. J., Rodríguez-Tovar, F. J., Llave, E., Ng, Z. L., Nishida, N., & Mena, A. (2020). Contourites and bottom current reworked sands: Bed facies model and implications. *Marine Geology*, 428, 106267.
- Doré, A., Lundin, E., Jensen, L., Birkeland, Ø., Eliassen, P., & Fichler, C. (1999). Principal tectonic events in the evolution of the northwest European Atlantic margin. In *Proceedings geological society, London, petroleum geology conference series* (Vol. 5, pp. 41–61). Geological Society of London.
- Doré, A., Lundin, E., Kuszniir, N., & Pascal, C. (2008). Potential mechanisms for the genesis of Cenozoic domal structures on the NE Atlantic margin: Pros, cons and some new ideas. *Geological Society, London, Special Publications*, 306(1), 1–26.
- Dutton, S. P., White, C. D., Willis, B. J., & Novakovic, D. (2002). Calcite cement distribution and its effect on fluid flow in a deltaic sandstone, frontier formation, Wyoming. *AAPG Bulletin*, 86(12), 2007–2021.
- Eberli, G. P., Bernoulli, D., Vecsei, A., Sekti, R., Grasmueck, M., Lüdmann, T., Anselmetti, F. S., Mutti, M., & Porta, G. D. (2019). A Cretaceous carbonate delta drift in the Montagna della Maiella, Italy. *Sedimentology*, 66(4), 1266–1301.
- Eberli, G. P., & Betzler, C. (2019). Characteristics of modern carbonate contourite drifts. *Sedimentology*, 66(4), 1163–1191.
- Eldholm, O. (1991). Magmatic tectonic evolution of a volcanic rifted margin. *Marine Geology*, 102(1–4), 43–61.
- Eldholm, O., & Grue, K. (1994). North Atlantic volcanic margins: Dimensions and production rates. *Journal of geophysical research: Solid Earth*, 99(B2), 2955–2968.
- Faugères, J.-C., & Mulder, T. (2011). *Contour currents and contourite drifts, developments in sedimentology* (Vol. 63, pp. 149–214). Elsevier.
- Fonneland, H. C., Lien, T., Martinsen, O. J., Pedersen, R. B., & Košler, J. (2004). Detrital zircon ages: A key to understanding the deposition of deep marine sandstones in the Norwegian Sea. *Sedimentary Geology*, 164(1–2), 147–159.
- Fonnesu, M., Palermo, D., Galbiati, M., Marchesini, M., Bonamini, E., & Bendias, D. (2020). A new world-class deep-water play-type, deposited by the syndepositional interaction of turbidity flows and bottom currents: The giant Eocene Coral Field in northern Mozambique. *Marine and Petroleum Geology*, 111, 179–201.
- Gaina, C., Gernigon, L., & Ball, P. (2009). Palaeocene–Recent plate boundaries in the NE Atlantic and the formation of the Jan Mayen microcontinent. *Journal of the Geological Society*, 166(4), 601–616.
- Gernigon, L., Franke, D., Geoffroy, L., Schiffer, C., Foulger, G. R., & Stoker, M. (2019). Crustal fragmentation, magmatism, and the diachronous opening of the Norwegian–Greenland Sea. *Earth-Science Reviews*, 206, 102839.
- Gernigon, L., Gaina, C., Olesen, O., Ball, P., Péron-Pinvidic, G., & Yamasaki, T. (2012). The Norway Basin revisited: From continental breakup to spreading ridge extinction. *Marine and Petroleum Geology*, 35(1), 1–19.
- Gernigon, L., Zastozhnov, D., Planke, S., Manton, B., Abdelmalak, M. M., Olessen, O., Maharjan, D., Faleide, J. I., & Myklebust, R. (2021). A digital compilation of structural and magmatic elements of the Mid-Norwegian continental margin (version 1.0). *Norwegian Journal of Geology*, 101, 1–74.
- Goodchild, M., Henry, K., Hinkley, R., & Imbus, S. (1999). The victory gas field, west of Shetland. In *Proceedings geological society, London, Petroleum Geology Conference series* (Vol. 5, pp. 713–724). Geological Society of London.
- Grunnalleite, I., & Gabrielsen, R. H. (1995). Structure of the Møre Basin, mid-Norway continental margin. *Tectonophysics*, 252(1–4), 221–251.
- Handford, C. R., & Loucks, R. G. (1993). Carbonate depositional sequences and systems tracts—responses of carbonate platforms to relative sea-level changes: Chapter 1. In *AAPG Memoir, carbonate sequence stratigraphy: Recent developments and applications*. AAPG.
- Helland-Hansen, W., Sømme, T. O., Martinsen, O. J., Lunt, I., & Thurmond, J. (2016). Deciphering Earth's natural hourglasses: Perspectives on source-to-sink analysis. *Journal of Sedimentary Research*, 86(9), 1008–1033.
- Kjennerud, T., & Vergara, L. (2005). Cretaceous to Palaeogene 3D palaeobathymetry and sedimentation in the Vøring Basin, Norwegian Sea. In *Proceedings Geological Society London, Petroleum Geology Conference series* (Vol. 6, pp. 815–831). Geological Society of London.
- Kjoberg, S., Schmiedel, T., Planke, S., Svensen, H. H., Millett, J. M., Jerram, D. A., Galland, O., Lecomte, I., Schofield, N., &

- Haug, Ø. T. (2017). 3D structure and formation of hydrothermal vent complexes at the Paleocene-Eocene transition, the Møre Basin, mid-Norwegian margin. *Interpretation*, 5(3), SK65–SK81.
- Lamers, E., & Carmichael, S. (1999). The Paleocene deepwater sandstone play West of Shetland. In *Proceedings Geological Society, London, Petroleum geology conference series* (Vol. 5, pp. 645–659). Geological Society of London.
- Lebedeva-Ivanova, N., Polteau, S., Bellwald, B., Planke, S., Berndt, C., & Stokke, H. H. (2018). Toward one-meter resolution in 3D seismic. *The Leading Edge*, 37(11), 818–828.
- Loucks, R. G., Kerans, C., Janson, X., Rojano, M. M., Shipp, R., Weimer, P., & Posamentier, H. (2011). Lithofacies analysis and stratigraphic architecture of a deep-water carbonate debris apron: Lower Cretaceous (latest Aptian to latest Albian) Tamabra Formation, Poza Rica field area, Mexico. In *Mass-transport deposits in deepwater settings* (pp. 367–390). SEPM (Society for Sedimentary Geology) Special Publication.
- Mahdi, S., & Ayress, M. (2006). *A biostratigraphical evaluation of the Pleistocene to Late Cretaceous interval in well 6302/6-1, Tulipan Prospect, NOCS*. Ichron/Statoil.
- Martinsen, O., Lien, T., & Jackson, C. (2005). Cretaceous and Palaeogene turbidite systems in the North Sea and Norwegian Sea Basins: Source, staging area and basin physiography controls on reservoir development. In *Proceedings Geological Society, London, Petroleum Geology Conference series* (Vol. 6, pp. 1147–1164). Geological Society of London.
- Millett, J. M., Manton, B. M., Zastrozhnov, D., Planke, S., Maharjan, D., Bellwald, B., Gernigon, L., Faleide, J. I., Jolley, D. W., & Walker, F. (2022). Basin structure and prospectivity of the NE Atlantic volcanic rifted margin: Cross-border examples from the Faroe–Shetland, Møre and Southern Vøring basins. *Geological Society, London, Special Publications*, 495(1), SP495-2019-2012.
- Moraes, M. A. S., Maciel, W. B., Braga, M. S. S., & Viana, A. R. (2007). Bottom-current reworked Palaeocene-Eocene deep-water reservoirs of the Campos Basin, Brazil. *Geological Society Special Publication*, 276, 81–94.
- Mosar, J., Eide, E. A., Osmundsen, P. T., Sommaruga, A., & Torsvik, T. H. (2002). Greenland–Norway separation: A geodynamic model for the North Atlantic. *Norwegian Journal of Geology*, 82, 282.
- Mount, J. (1985). Mixed siliciclastic and carbonate sediments: A proposed first-order textural and compositional classification. *Sedimentology*, 32(3), 435–442.
- Mullins, H. T., & Cook, H. E. (1986). Carbonate apron models: Alternatives to the submarine fan model for paleoenvironmental analysis and hydrocarbon exploration. *Sedimentary Geology*, 48(1–2), 37–79.
- Payros, A., & Pujalte, V. (2008). Calciclastic submarine fans: An integrated overview. *Earth-Science Reviews*, 86(1), 203–246.
- Peron-Pinvidic, G., Gernigon, L., Gaina, C., & Ball, P. (2012). Insights from the Jan Mayen system in the Norwegian-Greenland Sea-II. Architecture of a microcontinent. *Geophysical Journal International*, 191(2), 413–435.
- Peron-Pinvidic, G., & Osmundsen, P. T. (2018). The Mid Norwegian-NE Greenland conjugate margins: Rifting evolution, margin segmentation, and breakup. *Marine and Petroleum Geology*, 98, 162–184.
- Picot, M., Droz, L., Marsset, T., Dennielou, B., & Bez, M. (2016). Controls on turbidite sedimentation: Insights from a quantitative approach of submarine channel and lobe architecture (Late Quaternary Congo Fan). *Marine and Petroleum Geology*, 72, 423–446.
- Planke, S., Berndt, C., & Alvarez Zarikian, C. A. (2022). *International Ocean discovery program expedition 396 preliminary report mid-Norwegian margin magmatism and paleoclimate implications*. International Ocean Discovery Program (IODP). <https://doi.org/10.14379/iodp.pr.396.2022>
- Playton, T. E., Janson, X., & Kerans, C. (2011). Carbonate slopes. In N. P. James & R. W. Dalrymple (Eds.), *Facies models* (Vol. 4, pp. 449–476). Geoscience Canada.
- Podladchikov, Y., Rüpke, L., Schmalholz, S., & Simon, N. (2006). Late syn-rift (65–55 Ma) uplift in the Voring Basin, Norwegian Sea—was it a ‘hot’ or a ‘cold’ event? In *Proceedings AGU Fall Meeting Abstracts* (Vol. 2006, T52C-04). AGU.
- Polanco, S., Blum, M., Salles, T., Frederick, B. C., Farrington, R., Ding, X., Mather, B., Mallard, C., & Moresi, L. (2023). The flexural isostatic response of climatically driven sea-level changes on continental-scale deltas. *EGUSphere*, 2023, 1–30.
- Polteau, S., Mazzini, A., Hansen, G., Planke, S., Jerram, D. A., Millett, J., Abdelmalak, M. M., Blischke, A., & Myklebust, R. (2019). The pre-breakup stratigraphy and petroleum system of the Southern Jan Mayen Ridge revealed by seafloor sampling. *Tectonophysics*, 760, 152–164.
- Ravnås, R., Nøttvedt, A., Steel, R., & Windelstad, J. (2000). Syn-rift sedimentary architectures in the Northern North Sea. *Geological Society, London, Special Publications*, 167(1), 133–177.
- Ravnås, R., & Steel, R. (1997). Contrasting styles of Late Jurassic syn-rift turbidite sedimentation: A comparative study of the Magnus and Oseberg areas, northern North Sea. *Marine and Petroleum Geology*, 14(4), 417–449.
- Ravnås, R., & Steel, R. (1998). Architecture of Marine Rift-Basin successions. *AAPG Bulletin*, 82(1), 110–146.
- Rebesco, M., Hernández-Molina, F. J., Van Rooij, D., & Wåhlin, A. (2014). Contourites and associated sediments controlled by deep-water circulation processes: State-of-the-art and future considerations. *Marine Geology*, 352, 111–154.
- Reijmer, J. J., Palmieri, P., Groen, R., & Floquet, M. (2015). Calciturbidites and calcidebrites: Sea-level variations or tectonic processes? *Sedimentary Geology*, 317, 53–70.
- Reolid, J., Betzler, C., & Lüdmann, T. (2019). Facies and sedimentology of a carbonate delta drift (Miocene, Maldives). *Sedimentology*, 66(4), 1243–1265.
- Roberts, A. M., Corfield, R. I., Kusznir, N. J., Matthews, S. J., Hansen, E.-K., & Hooper, R. J. (2009). Mapping palaeostructure and palaeobathymetry along the Norwegian Atlantic continental margin: Møre and Vøring basins. *Petroleum Geoscience*, 15(1), 27–43.
- Schlager, W., Reijmer, J. J., & Droxler, A. (1994). Highstand shedding of carbonate platforms. *Journal of Sedimentary Research*, 64(3b), 270–281.
- Schmiedel, T., Kjøberg, S., Planke, S., Magee, C., Galland, O., Schofield, N., Jackson, C. A.-L., & Jerram, D. A. (2017). Mechanisms of overburden deformation associated with the emplacement of the Tulipan sill, mid-Norwegian margin. *Interpretation*, 5(3), SK23–SK38.
- Scholle, P. A., Albrechtsen, T., & Tirsgaard, H. (1998). Formation and diagenesis of bedding cycles in uppermost Cretaceous chalks of the Dan Field, Danish North Sea. *Sedimentology*, 45(2), 223–243.

- Simm, R., & Bacon, M. (2014). *Seismic amplitude: An interpreter's handbook*. Cambridge University Press.
- Skogseid, J., & Eldholm, O. (1987). Early Cenozoic crust at the Norwegian continental margin and the conjugate Jan Mayen Ridge. *Journal of geophysical research: Solid Earth*, 92(B11), 11471–11491.
- Skogseid, J., Planke, S., Faleide, J. I., Pedersen, T., Eldholm, O., & Neverdal, F. (2000). NE Atlantic continental rifting and volcanic margin formation. *Geological Society, London, Special Publications*, 167(1), 295–326.
- Slootman, A., De Boer, P. L., Cartigny, M. J., Samankassou, E., & Moscarriello, A. (2019). Evolution of a carbonate delta generated by gateway-funnelling of episodic currents. *Sedimentology*, 66(4), 1302–1340.
- Sømme, T. O., Huwe, S. I., Martinsen, O. J., Sandbakken, P. T., Skogseid, J., & Valore, L. A. (2023). Stratigraphic expression of the Paleocene-Eocene Thermal Maximum climate event during long-lived transient uplift—An example from a shallow to deep-marine clastic system in the Norwegian Sea. *Frontiers in Earth Science*, 11, 1–30.
- Sømme, T. O., Skogseid, J., Embry, P., & Løseth, H. (2019). Manifestation of tectonic and climatic perturbations in deep-time stratigraphy—an example from the Paleocene succession offshore western Norway. *Frontiers in Earth Science*, 7, 303.
- Southern, S. J., Kane, I. A., Warchoř, M. J., Porten, K. W., & McCaffrey, W. D. (2017). Hybrid event beds dominated by transitional-flow facies: Character, distribution and significance in the Maastrichtian Springar Formation, north-west Vøring Basin, Norwegian Sea. *Sedimentology*, 64(3), 747–776.
- Stoker, M. S. (2016). Cretaceous tectonostratigraphy of the Faroe–Shetland region. *Scottish Journal of Geology*, 52(1), 19–41.
- Stokke, E. W., Jones, M. T., Riber, L., Haflidason, H., Midtkandal, I., Schultz, B. P., & Svensen, H. H. (2021). Rapid and sustained environmental responses to global warming: The Paleocene–Eocene Thermal Maximum in the eastern North Sea. *Climate of the Past*, 17(5), 1989–2013.
- Surlyk, F., Dons, T., Clausen, C. K., & Higham, J. (2003). Upper cretaceous. *The Millennium Atlas: Petroleum Geology of the Central and Northern North Sea*. Geological Society, London, 213, 233.
- Surlyk, G. (1997). A cool-water carbonate ramp with bryozoan mounds: Late Cretaceous–Danian of the Danish Basin. *Special Publication-SEPM*, 56, 293–308.
- Talling, P. J., Masson, D. G., Sumner, E. J., & Malgesini, G. (2012). Subaqueous sediment density flows: Depositional processes and deposit types. *Sedimentology*, 59(7), 1937–2003.
- Theissen-Krah, S., Zastrozhnov, D., Abdelmalak, M., Schmid, D., Faleide, J., & Gernigon, L. (2017). Tectonic evolution and extension at the Møre Margin–Offshore mid-Norway. *Tectonophysics*, 721, 227–238.
- Triplehorn, D. M. (1966). Morphology, internal structure, and origin of glauconite pellets. *Sedimentology*, 6(4), 247–266.
- Tropeano, M., Spalluto, L., Meloni, D., Moretti, M., & Sabato, L. (2022). ‘Isolated base-of-slope aprons’: An oxymoron for shallow-marine fan-shaped, temperate-water, carbonate bodies along the south-East Salento escarpment (Pleistocene, Apulia, southern Italy). *Sedimentology*, 69(1), 345–371.
- Vergara, L., Wreglesworth, I., Trayfoot, M., & Richardsen, G. (2001). The distribution of Cretaceous and Paleocene deep-water reservoirs in the Norwegian Sea basins. *Petroleum Geoscience*, 7(4), 395–408.
- Walker, F., Schofield, N., Millett, J., Jolley, D., Planke, S., & Holford, S. (2022). Paleogene drainage system evolution in the NE Faroe-Shetland Basin. *Journal of the Geological Society*, 179. <https://doi.org/10.1144/jgs2021-121>
- Wien, S. T., & Kjennerud, T. (2005). 3D cretaceous to Cenozoic palaeobathymetry of the northern North Sea. In *Norwegian petroleum society special publications* (Vol. 12, pp. 241–253). Elsevier.
- Zastrozhnov, D., Gernigon, L., Gogin, I., Planke, S., Abdelmalak, M. M., Polteau, S., Faleide, J. I., Manton, B., & Myklebust, R. (2020). Regional structure and polyphased Cretaceous–Paleocene rift and basin development of the mid-Norwegian volcanic passive margin. *Marine and Petroleum Geology*, 115, 104269.
- Zuffa, G. G. (1980). Hybrid arenites; their composition and classification. *Journal of Sedimentary Research*, 50(1), 21–29.

How to cite this article: Kjöll, H. J., Midtkandal, I., Planke, S., Millett, J., Manton, B., & Anderskov, K. (2023). The interplay between siliciclastic and carbonate depositional systems: Maastrichtian to Danian basin-floor sediments of the mid-Norwegian Møre Basin. *Basin Research*, 00, 1–31. <https://doi.org/10.1111/bre.12827>

APPENDIX 1

Formal Definition of the Grisetang Member

Occurrence	Møre Basin, Norwegian Sea
Status of unit	Formal
First use of name	This contribution
Current definition	Present paper based on data from well 6302/6-1
Synonym and reference	None
Origin of name	Norwegian name for a specific seaweed (tang)
Type section	Well 6302/6-1
Hypostratotype	...
Depositional age	Maastrichtian—Danian
Dating methods and reference(s) for age	Biostratigraphy presented in Mahdi and Ayress (2006)
Overlying unit	Mudstone of the Sautang Member (see Appendix 2 , this contribution)
Underlying unit	Mudstones of the Springar Formation
Superior unit	Tang Formation
Other use of name	Seaweed
Thickness	65 m in well
Main lithologies	Chalk, sandstone, mudstone
Lower boundary definition	The lower boundary is defined by the Base Paleogene Unconformity and the mudstones of the Springar Formation, which in the type locality corresponds to a negative impedance contrast
Description	The Grisetang Member is recognized in well 6302/6-1 in the Møre Basin in the Norwegian Sea. It can be mapped in the 3D seismic cube ST0105, BG0805 and AMS-18. At the time of writing the Grisetang Member has only occurred in the reference well. The member comprise 5 carbonate beds thicker than 1 m, interlayered by mudstones. The base of the lowermost carbonate bed comprise coarser fossiliferous limestone, whereas the remainder of the bed, like the other beds comprise very fine grained micritic carbonate. The top of the two topmost carbonate beds comprise clean, quartz-rich sandstones with wireline log characteristics similar to the carbonates

APPENDIX 2

Formal Definition of Sautang Member

Occurrence	Møre Basin, Norwegian Sea
Status of unit	Formal
First use of name	This contribution
Current definition	Present paper based on data from well 6302/6-1
Synonym and reference	None
Origin of name	Norwegian name for a specific seaweed (tang)
Type section	Well 6302/6-1
Hypostratotype	...
Depositional age	Danian
Dating methods and reference(s) for age	Biostratigraphy presented in Mahdi and Ayress (2006)
Overlying unit	Sandstones of the Sautang Member (see Appendix 3 , this contribution)
Underlying unit	Carbonates of the Grisetang Member

Occurrence	Møre Basin, Norwegian Sea
Superior unit	Tang Formation
Other use of name	Seaweed
Thickness	77 m in well
Main lithologies	Mudstone and minor sandstone
Lower boundary definition	The lower boundary is defined by the first occurrence of a carbonate bed belonging to the Grisatang Member (see Appendix 1 , this contribution)
Description	The Sautatang Member is recognized in well 6302/6-1 in the Møre Basin in the Norwegian Sea. It can be mapped in the 3D seismic cube ST0105, BG0805 and AMS-18. The member is primarily comprised of mudstone with sandstone stringers that range in thickness in the reference well from c. 1.5 to 0.3 m. The sandstone stringers have erosional bases and often display dewatering structures. The mudstones are generally laminated and/or bioturbated

APPENDIX 3

Formal Definition of the Sagtang Member

Occurrence	Møre Basin, Norwegian Sea
Status of unit	Formal
First use of name	This contribution
Current definition	Present paper based on data from well 6302/6-1
Synonym and reference	None
Origin of name	Norwegian name for a specific seaweed (tang)
Type section	Well 6302/6-1
Hypostratotype	...
Depositional age	Danian
Dating methods and reference(s) for age	Biostratigraphy presented in Mahdi and Ayres (2006)
Overlying unit	Mudstones of the Tang Formation (see Appendix 3 , this contribution)
Underlying unit	Mudstones of the Sautatang Member
Superior unit	Tang Formation
Other use of name	Seaweed
Thickness	96 m in well
Main lithologies	Sandstone, mudstone
Lower boundary definition	The lower boundary is defined by the first occurrence of a mudstone bed belonging to the Sautatang Member (see Appendix 2 , this contribution)
Description	The Sautatang Member is recognized in well 6302/6-1 in the Møre Basin in the Norwegian Sea. It can be mapped in the 3D seismic cube ST0105, BG0805 and AMS-18. The member is primarily comprised of sandstone beds interlayered by mudstones. The sandstone beds range in thickness in the reference well from c. 1.5 to 0.3 m. The sandstone beds have erosional bases and often display dewatering structures. The mudstones are often present as heteroliths. Proper mudstone beds in the member are generally laminated and/or bioturbated. The uppermost sandstone beds are, in the study area, often gas-charged and can be mapped based on the negative change in acoustic impedance from the overlying mudstones to the gas-charged sandstones